Check for updates

Small

NANO · MICRO small
www.small-journal.com

RESEARCH ARTICLE OPEN ACCESS

NaCl-Templated Iron Sulfide/N-Doped Carbon Microspheres for High-Performance Sodium-Ion Batteries: From Nanostructural Design to Pouch Cells

Ji Myeon Park[1,2] | Hyojun Lim[3,4,5] | Ju Young Kim[6] | Weiyin Chen[3,7] | Jin Hyeong Lee[1,2] | Seul Jeong[1,2] | Hwa Young Choi[1,2] | Jaekyung Sung[4] | Yun Chan Kang[6] | Ju Li[3,7] | Jin-Sung Park[1,2]

[1]Department of Materials Science and Engineering, Ajou University, Suwon, Republic of Korea | [2]Department of Energy Systems Research, Ajou University, Suwon, Republic of Korea | [3]Department of Nuclear Science and Engineering, Massachusetts Institute of Technology, Cambridge, Massachusetts, USA | [4]Department of Materials Engineering and Convergence Technology and RIMA, Gyeongsang National University, Jinju, Republic of Korea | [5]Energy Storage Research Department, Korea Institute of Energy Research (KIER), Daejeon, Republic of Korea | [6]Department of Materials Science and Engineering, Korea University, Seoul, Republic of Korea | [7]Department of Materials Science and Engineering, Massachusetts Institute of Technology, Cambridge, Massachusetts, USA

Correspondence: Yun Chan Kang (yckang@korea.ac.kr) | Ju Li (liju@mit.edu) | Jin-Sung Park (jinsung@ajou.ac.kr)

Received: 4 June 2026 | **Revised:** 13 August 2026 | **Accepted:** 30 September 2026

Keywords: hierarchical porous structure | iron sulfide | N-doped carbon | Sodium-ion batteries | spray pyrolysis

ABSTRACT

In this study, we report the rational design of NaCl-templated iron sulfide/N-doped carbon (FeS-NaCl@NC) microspheres as high-performance anodes for sodium-ion batteries. A scalable spray pyrolysis process combined with subsequent sulfidation and polydopamine-derived carbon coating enables the formation of three-dimensional (3D) interconnected porous architectures with conformal N-doped carbon layers. The NaCl template plays a critical role in generating internal void networks and mesoporous structures, facilitating electrolyte penetration and shortening Na^+ diffusion pathways, while the N-doped carbon coating enhances electronic conductivity and interfacial stability. As a result, FeS-NaCl@NC microspheres exhibit outstanding electrochemical performance, maintaining a high discharge capacity of 576.3 mA h g^{-1} after 100 cycles at 1.0 A g^{-1} and delivering remarkable rate capability (251.7 mA h g^{-1} at 10.0 A g^{-1}). Notably, the improved cycling stability is rationalized by nano-indentation results, indicating enhanced mechanical resilience against repeated volume changes. In addition, the origin of the superior rate capability is comprehensively elucidated through combined electrochemical and kinetic analyses, confirming that the designed structure enables accelerated Na^+ transport and charge transfer. Moreover, the practical feasibility of FeS-NaCl@NC microspheres is validated through pouch-type full-cell evaluation, demonstrating its strong potential for sodium-ion storage applications.

1 | Introduction

The increasing demand for large-scale energy storage systems has accelerated the development of cost-effective and sustainable alternatives to the currently dominant lithium-ion batteries (LIBs) [1–3]. Among various candidates, sodium-ion batteries (SIBs) have emerged as promising systems owing to the natural abundance and low cost of sodium resources, as well as their similar electrochemical characteristics to LIBs [4, 5]. However, the larger ionic radius and sluggish diffusion kinetics of Na^+

Ji Myeon Park, Hyojun Lim and Ju Young Kim contributed equally to this work.

This is an open access article under the terms of the Creative Commons Attribution License, which permits use, distribution and reproduction in any medium, provided the original work is properly cited.
© 2026 The Author(s). *Small* published by Wiley-VCH GmbH

ions impose significant challenges in achieving high capacity and long-term cycling stability [6]. Metal chalcogenides have attracted considerable attention as high-capacity anode materials for SIBs due to their conversion reaction mechanism that leads to high theoretical capacities [7–9]. Nevertheless, their practical application is hindered by severe volume expansion, structural pulverization, and poor intrinsic electrical conductivity during repeated sodiation/desodiation processes [10, 11]. These issues result in rapid capacity fading and limited rate capability, necessitating rational structural and compositional design strategies [12, 13].

To address these challenges, previous studies have focused on incorporating metal sulfides with conductive carbon matrices and engineering hierarchical nanostructures such as porous, hollow, and yolk-shell architectures [14–17]. Such approaches effectively buffer volume changes, enhance electrical conductivity, and improve electrolyte accessibility [18, 19]. Recent studies have further demonstrated that synergistic structural and compositional engineering can effectively enhance reaction kinetics and cycling stability of metal chalcogenide anodes [20–22]. However, many of these strategies rely on complicated multi-step synthesis routes or sacrificial templates that require harsh chemical etching or high-temperature treatment for removal, leading to increased process complexity and limited scalability [23].

In this context, template-assisted spray-based synthesis has emerged as an attractive strategy for constructing structurally robust and scalable electrode materials [24]. Building upon this concept, we developed a uniquely structured metal sulfide/carbon composite microsphere system featuring NaCl-assisted porous architecture and subsequent N-doped carbon coating, enabling both structural stability and enhanced electrochemical kinetics. NaCl-templated framework generates internal voids and 3-dimensionally interconnected porous ion diffusion channels, while the N-doped carbon layer, which is coated conformally on the surface of the porous superstructure, improves electronic conductivity and interfacial stability [25].

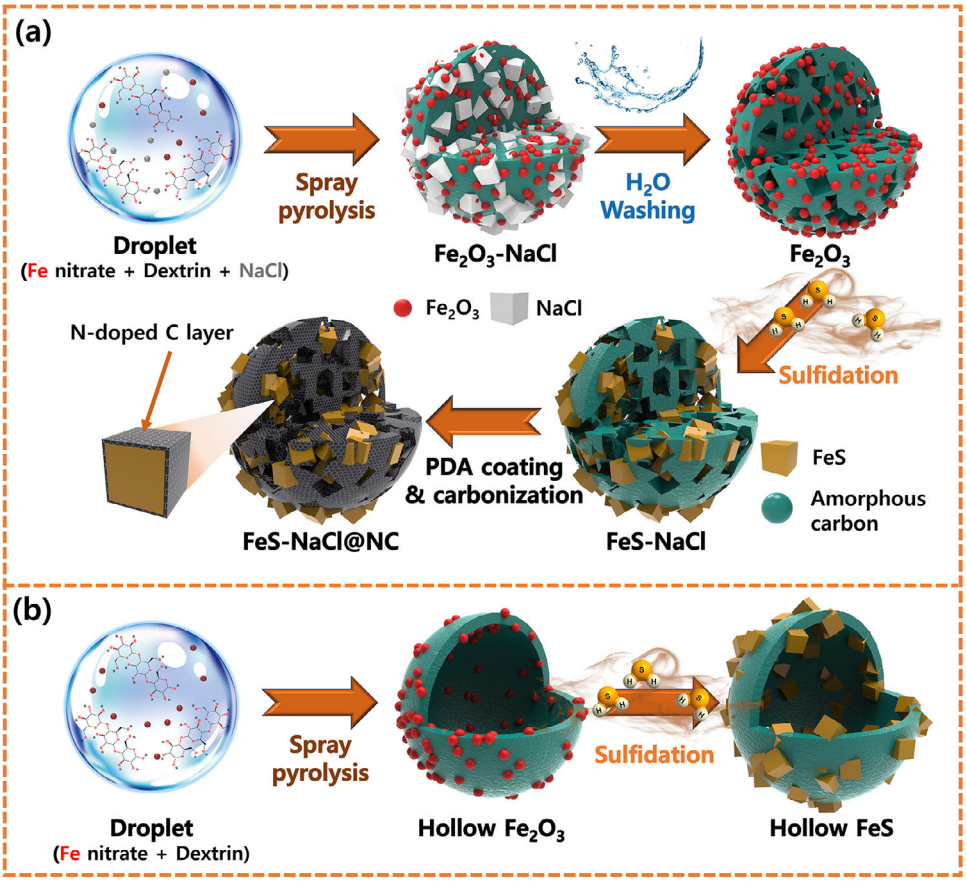
As a representative system, Fe-based sulfide composites with controlled phase composition (e.g., FeS_2/Fe_7S_8) and hierarchical porosity were synthesized via a scalable spray pyrolysis process. The resulting structure provides multiple advantages, including shortened Na^+ diffusion pathways, improved electrolyte penetration, and effective accommodation of volume changes during cycling. The origin of the structural stability of the prepared microspheres is elucidated via various techniques, including nano-indentation and cross-sectional scanning electron microscopy (SEM) analyses. Importantly, beyond conventional half-cell evaluations, we further assessed the practical applicability of the developed materials by assembling a pouch-type sodium-based full-cell. This evaluation demonstrates the feasibility of our material design under realistic operating conditions, bridging the gap between laboratory-scale performance and practical energy storage applications.

2 | Results and Discussions

The schematic diagram illustrating the formation mechanism of nanostructured iron sulfide composited with 3D interconnected void architecture formed from NaCl nanoparticles with cubic morphology, which is further coated with a thin N-doped carbon layer, is shown in Scheme 1a. First, iron nitrate, NaCl, and dextrin were dissolved in distilled water to form a transparent solution, which was then atomized using an ultrasonic nebulizer to generate micron-sized droplets. The droplets were transferred to the furnace due to the nitrogen gas flow (which acts as the carrier gas), which were then dried and pyrolyzed to form composite microspheres comprised of Fe_2O_3, NaCl, and carbon due to the decomposition of iron nitrate and carbonization of dextrin. Centrifuging of the spray-pyrolyzed powder washed away the NaCl nanoparticles embedded in the microsphere, which resulted in the formation of 3D interconnected internal void networks. Subsequently, the powder went through a sulfidation process using thiourea as the sulfur source under a reducing gas atmosphere, which resulted in the formation of FeS-NaCl microspheres. To reinforce the electrical and mechanical properties of the prepared microspheres, the powder was further coated with N-doped carbon layer, which can form a thin and highly conformal coating layer on the surface of the 3D porous framework. Sodium ion storage performance of two control samples was also tested for comparison purpose: (1) FeS-NaCl microspheres with 3D internal void space originated from NaCl, but without N-doped carbon coating, and (2) Hollow FeS microspheres prepared from the spray solution that does not contain NaCl.

Figure 1 presents the morphological, structural, and compositional characterization of iron sulfide/carbon composite microspheres featuring a three-dimensional porous structure, constructed via NaCl templating during spray pyrolysis. The SEM images of Fe_2O_3-NaCl composite microsphere prepared directly from spray pyrolysis (Figure 1a and Figure S1) reveal independent microspherical morphology without any aggregation between the particles. The SEM images clearly show NaCl nanoparticles decorating the microsphere surfaces prior to removal. The morphology of Fe_2O_3-carbon composites after washing with distilled water is shown in Figure 1b, which reveals that NaCl nanoparticles act as a sacrificial template, which results in the generation of 3D porous features, as evidenced by the internal void structure. The x-ray diffraction (XRD) patterns of Fe_2O_3-NaCl before and after the distilled water washing process clearly show that NaCl particles are removed after washing (Figure S2). The corresponding SEM-energy-dispersive x-ray spectroscopy (EDS) elemental mapping images reveal intense and broadly distributed Na and Cl signals throughout the Fe_2O_3-NaCl microspheres before washing, whereas both signals are markedly reduced after washing while the Fe-containing porous framework is retained (Figure S3). Quantitative EDS analysis further shows that the Na and Cl contents decreased from 8.7 and 5.7 at%, respectively, to approximately 0 at% after washing. These results demonstrate that the NaCl template is effectively removed to below the detection limits of the applied techniques. FeS-NaCl microspheres were prepared from a one-step sulfidation heat treatment, which reveals FeS particles with cubic morphology, which are anchored on the surface of 3D porous carbon framework (Figure 1c). The internal structure is further examined by transmission electron microscopy (TEM, Figure 1d,e), where the microspheres exhibit a highly porous architecture with interconnected void spaces. Thin carbon networks are observed throughout the structure, forming a continuous conductive matrix that is composited with iron sulfide domains. The presence of large internal voids

16136829, 0, Downloaded from https://onlinelibrary.wiley.com/doi/10.1002/smll.76162 by Massachusetts Institute of Technolo, Wiley Online Library on [08/11/2026]. See the Terms and Conditions (https://onlinelibrary.wiley.com/terms-and-conditions) on Wiley Online Library for rules of use; OA articles are governed by the applicable Creative Commons License



SCHEME 1 | Schematic illustration showing the formation mechanism of (a) FeS-NaCl@NC microspheres and (b) Hollow FeS microspheres.

is expected to effectively buffer the volume expansion during sodiation/desodiation processes while facilitating electrolyte penetration. High-resolution TEM (HR-TEM) analysis (Figure 1f) reveals the coexistence of multiple crystalline phases within the composite. Lattice fringes with spacings of ~0.24 and ~0.27 nm correspond to the (210) plane of pyrite-type FeS_2 and the (020) plane of marcasite FeS_2, respectively. This phase coexistence is further supported by the selected area electron diffraction (SAED) pattern (Figure 1g). Consistent with these observations, XRD patterns (Figure 1h) confirm the presence of both phases, showing characteristic peaks corresponding to pyrite-type FeS_2 (JCPDS No. 42–1340) and marcasite FeS_2 (JCPDS No. 37–0475). Raman spectroscopy (Figure 1i) shows two prominent peaks at approximately ~1350 cm^{-1} (D band) and ~1580 cm^{-1} (G band), corresponding to disordered and graphitic carbon, respectively [26, 27]. The calculated intensity ratio (I_D/I_G = 0.75) suggests a highly graphitized carbon structure, which can be attributed to the catalytic effect of Fe species during the carbonization process [28]. The elemental distribution within the microspheres is analyzed by EDS mapping (Figure 1j). Carbon element could be found throughout the entire microsphere, indicating the successful formation of carbon-composited iron-based sulfide microspheres. Sulfur and iron elements could also be observed throughout the microsphere, revealing that FeS particles are well composited with 3D carbon network. Notably, a homogeneous distribution of N element could also be observed in a single microsphere. The amounts of C and N were analyzed from the elemental analysis (EA) techniques, which revealed that there were 30.2% C and 13.0% N inside the microspheres (Table S1). The relatively high nitrogen content detected by EA is presumed to originate mainly from nitrogen-containing residues derived from the nitrate precursor and/or trapped surface species formed during spray pyrolysis and subsequent sulfidation [29, 30]. To clarify the origin of the unexpectedly high nitrogen content, additional EDS analysis was performed before and after DI-water washing. The nitrogen content of FeS-NaCl was 5.2 wt.% (5.6 at%) before washing, whereas nitrogen was no longer detected by EDS after washing, indicating that the nitrogen species located on or near the particle surface were effectively removed to a level below the detection capability of EDS (Table S2). This result supports the interpretation that the high nitrogen content was substantially influenced by water-removable nitrogen-containing residues formed during the thiourea-assisted sulfidation process.

Figure 2 presents a comprehensive structural and compositional characterization of 3D porous iron sulfide-carbon composite microspheres to which a thin N-doped carbon layer is coated. The SEM images (Figure 2a,b) reveal that the synthesized materials consist of well-defined spherical particles with an average diameter of 1.40 μm; the size distribution of the microspheres is shown in Figure S4. The spherical morphology with some degree of size distribution is beneficial in a way that it results in electrodes with high packing density. TEM analysis (Figure 2c,d) further confirms the formation of hollow/porous microspheres, where a thin and continuous carbon shell encapsulates the internal structure. The TEM image (Figure 2e) clearly shows the presence of an N-doped carbon coating layer, which conformally covers the surface of the iron sulfide nanocubes. HR-TEM imaging (Figure 2f) reveals

16136829, 0, Downloaded from https://onlinelibrary.wiley.com/doi/10.1002/smll.76162 by Massachusetts Institute of Technolo, Wiley Online Library on [08/11/2026]. See the Terms and Conditions (https://onlinelibrary.wiley.com/terms-and-conditions) on Wiley Online Library for rules of use; OA articles are governed by the applicable Creative Commons License

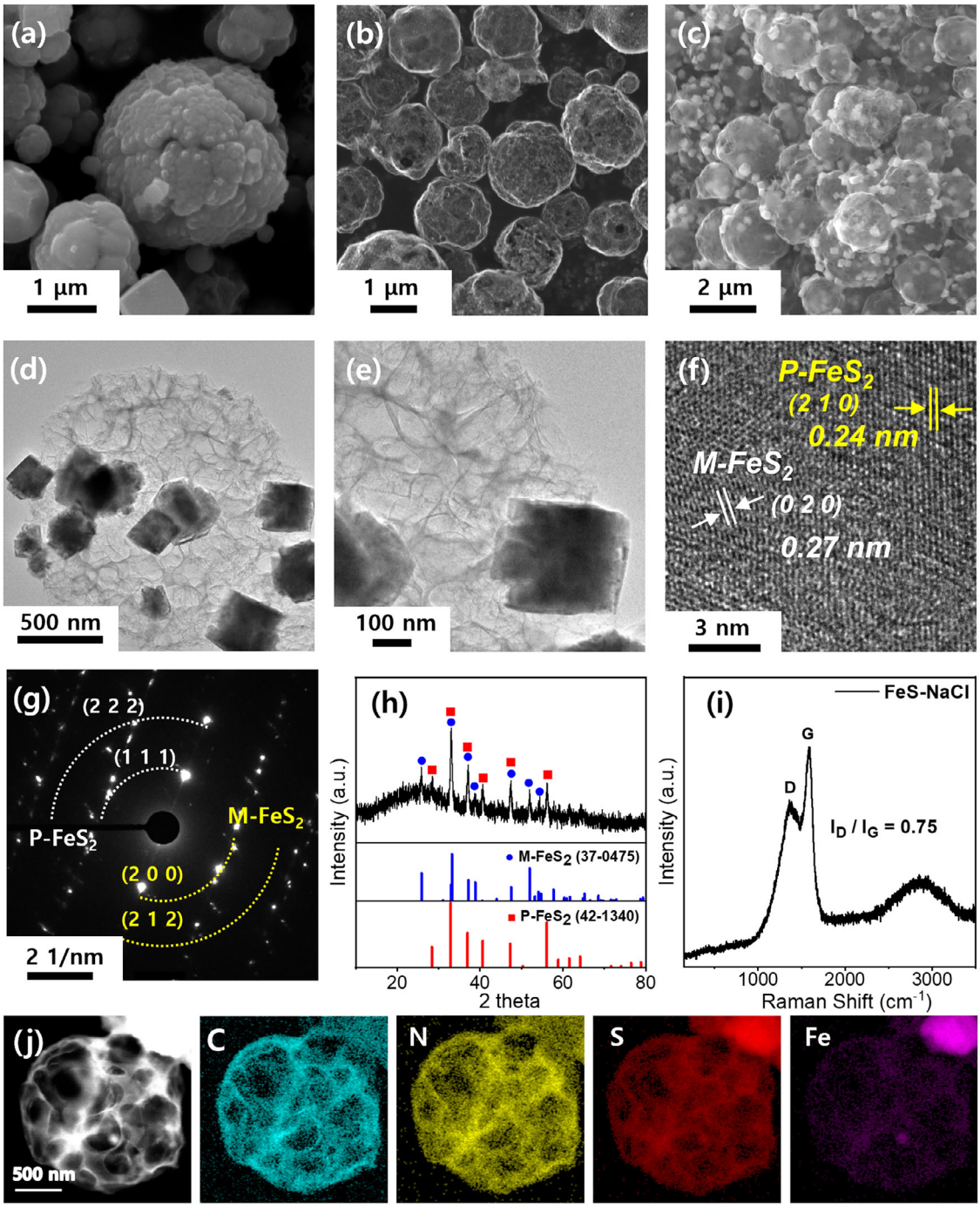


FIGURE 1 | (a) SEM image of Fe_2O_3-NaCl microspheres prepared directly from spray pyrolysis. (b) SEM image after washing the powder with distilled water. (c–j) Morphologies, SAED pattern, XRD pattern, Raman spectrum, and elemental mapping images of FeS-NaCl microspheres: (c) SEM image, (d,e) TEM image, (f) HR-TEM image, (g) SAED pattern, (h) XRD pattern, (i) Raman spectra, and (j) STEM-HAADF image and corresponding elemental dot mapping images.

distinct lattice fringes separated by the interplanar spacings of 0.28 nm and 0.15 nm, which can be indexed to the (006) plane of Fe_7S_8 and the (023) plane of FeS_2, respectively, indicating the coexistence of these two phases within the composite, which is further supported by the SAED patterns (Figure 2g). The XRD pattern (Figure 2h) shows characteristic peaks corresponding to pyrrhotite Fe_7S_8 (JCPDS No. 24–0220) and pyrite FeS_2 (JCPDS No. 42–1340) phases. Raman spectroscopy (Figure 2i) displays prominent D and G bands with the intensity ratio (I_D/I_G) of 0.78, which is slightly higher than that of the uncoated FeS-NaCl microspheres, probably due to the coating of N-doped carbon, which generally exhibits amorphous nature [31]. In addition, the heat treatment step for the carbonization of polydopamine is expected to form disordered carbon. Elemental mapping via EDS (Figure 2j) demonstrates a uniform distribution of C, N, S, and Fe throughout the microsphere, indicating the successful formation of iron sulfide nanocubes composited with 3D porous carbon microspheres.

16136829, 0, Downloaded from https://onlinelibrary.wiley.com/doi/10.1002/smll.76162 by Massachusetts Institute of Technolo, Wiley Online Library on [08/11/2026]. See the Terms and Conditions (https://onlinelibrary.wiley.com/terms-and-conditions) on Wiley Online Library for rules of use; OA articles are governed by the applicable Creative Commons License

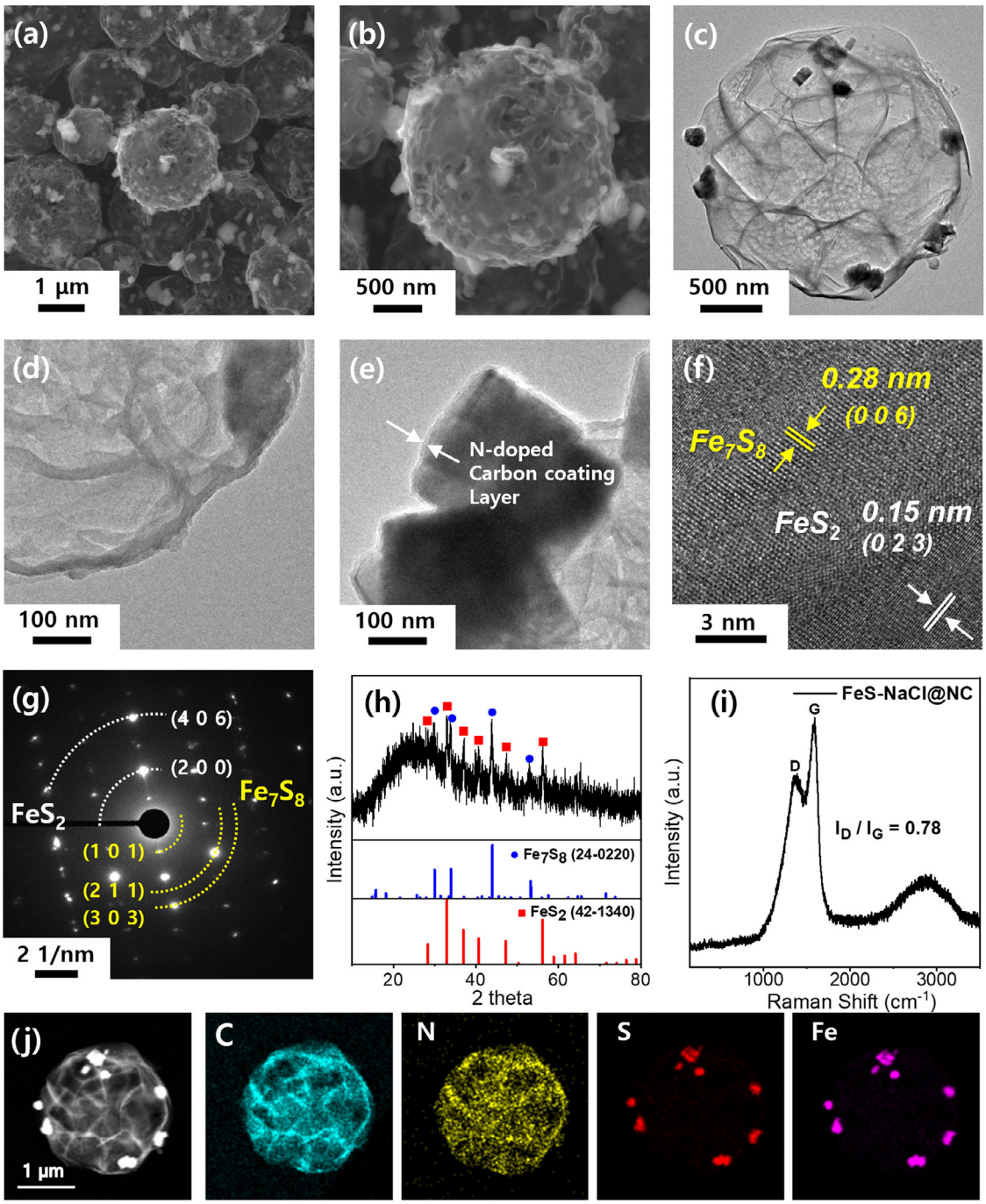


FIGURE 2 | Morphologies, SAED pattern, XRD pattern, and Raman spectrum, and elemental mapping images of FeS-NaCl@NC microspheres: (a,b) SEM image, (c–e) TEM image, (f) HR-TEM image, (g) SAED pattern, (h) XRD pattern, (i) Raman spectra, and (j) STEM-HAADF image and corresponding elemental dot mapping images.

For comparison purposes, a precursor solution that does not contain NaCl was spray pyrolyzed, which resulted in the formation of hollow Fe_2O_3 microspheres (Scheme 1b and Figure S5). The distinct morphological evolution of the microspheres can be attributed to the role of NaCl during the spray pyrolysis process. In the absence of NaCl, rapid solvent evaporation at the droplet surface induces the formation of a rigid outer shell at an early stage. This leads to a concentration gradient where solutes migrate toward the droplet surface, resulting in a typical "shell formation" mechanism [32]. In contrast, when NaCl is introduced into the precursor solution, it significantly alters the solute distribution and drying dynamics. Due to its high solubility and non-volatile nature, NaCl remains uniformly distributed throughout the droplet during evaporation and acts as a crystallization scaffold. This suppresses the rapid formation of a dense outer shell and instead promotes homogeneous precipitation of iron precursor and dextrin across the entire droplet volume. As a result, the particles solidify into filled microspheres rather than forming hollow ones. After the sulfidation of hollow Fe_2O_3 microspheres, FeS nanocrystals were embedded on the surface

16136829, 0, Downloaded from https://onlinelibrary.wiley.com/doi/10.1002/smll.76162 by Massachusetts Institute of Technolo, Wiley Online Library on [08/11/2026]. See the Terms and Conditions (https://onlinelibrary.wiley.com/terms-and-conditions) on Wiley Online Library for rules of use; OA articles are governed by the applicable Creative Commons License

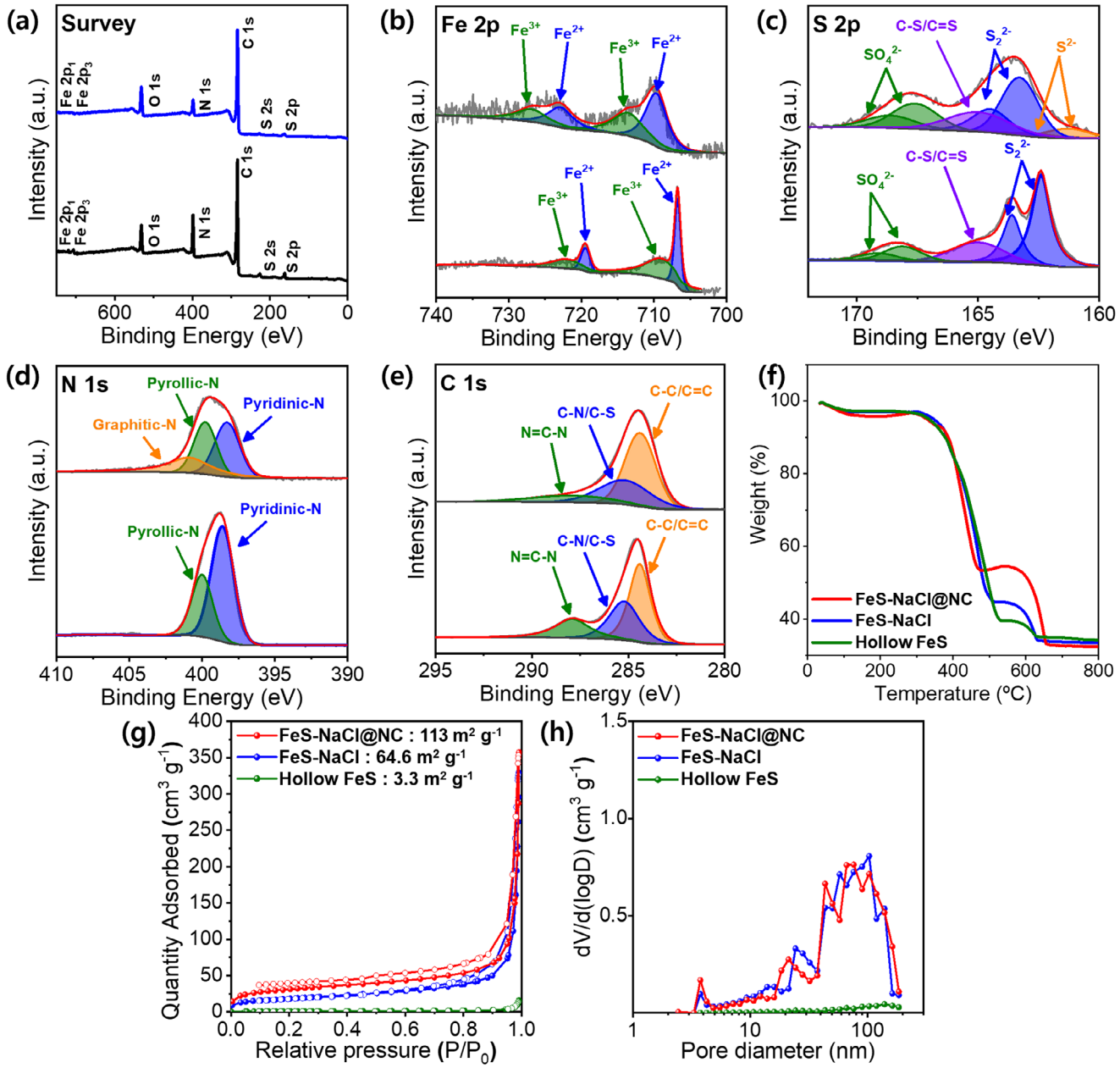


FIGURE 3 | Comprehensive material characterization of FeS-NaCl@NC, FeS-NaCl, and Hollow FeS microspheres. (a-e) XPS spectra: (a) survey, (b) Fe 2p, (c) S 2p, (d) N 1s, (e) C 1s spectra. (f) TGA curves. (g) N_2 adsorption–desorption isotherms and (h) BJH pore size distribution.

of carbon microspheres, as can be seen in the SEM image in Figure S6a,b. The XRD pattern in Figure S6c confirms that Hollow FeS microspheres exhibit marcasite FeS_2 (JCPDS No. 37–0475) and pyrite-type FeS_2 (JCPDS No. 42–1340) phases. The carbon and nitrogen contents in Hollow FeS microspheres analyzed by EA were 31.4% and 12.5%, respectively (Table S1). The Raman spectrum of Hollow FeS microspheres exhibits the I_D/I_G ratio of 0.76 (Figure S7), which indicates a moderately ordered carbon structure. This may be attributed to partial graphitization of the carbon matrix during thermal treatment in the presence of iron-based species [33].

The x-ray photoelectron spectroscopy (XPS) spectra of FeS-NaCl@NC and FeS-NaCl microspheres (top and bottom of the graphs, respectively) are shown in Figure 3a–e. The survey XPS spectra (Figure 3a) of both microspheres confirm the presence of Fe, S, C, N, and O elements. The Fe 2p spectra (Figure 3b) of the FeS-NaCl microspheres exhibit characteristic peaks associated with iron sulfide species. In particular, the Fe $2p_{3/2}$/Fe $2p_{1/2}$ peaks centered at ~706.7/719.4 eV are assigned to FeS_2 phase [34, 35]. Meanwhile, the broadened component observed at higher binding energies (709.0/722.1 eV) is attributed to Fe^{3+} species formed by surface oxidation [34, 35]. On the other hand, Fe 2p region for FeS-NaCl@NC microspheres can be deconvoluted into components assigned to FeS_2 and Fe_7S_8, confirming the formation of a FeS_2/Fe_7S_8 heterostructure after carbon coating. Notably, after the N-doped carbon coating, the peaks were broadened and slightly shifted to a higher binding energy (709.7/722.9 eV), suggesting interfacial electronic interaction between iron sulfide phases and the

16136829, 0, Downloaded from https://onlinelibrary.wiley.com/doi/10.1002/smll.76162 by Massachusetts Institute of Technolo, Wiley Online Library on [08/11/2026]. See the Terms and Conditions (https://onlinelibrary.wiley.com/terms-and-conditions) on Wiley Online Library for rules of use; OA articles are governed by the applicable Creative Commons License

N-doped carbon layer, which induces electron redistribution at the heterointerface [36]. Also, the additional component appearing at higher binding energy (713.6/726.9 eV) is attributed to Fe^{3+} species originating from Fe_7S_8 [37]. In the case of S 2p spectra in Figure 3c, the dominant peaks centered at 162.4 and 163.6 eV correspond to metal–sulfur bonds (S_2^{2-}), confirming the formation of Fe-S compounds [38]. Weak but noticeable peaks centered at 161.3 and 162.7 eV are observed in the N-doped carbon-coated sample, which can be attributed to the sulfur species in Fe_7S_8 [39]. In addition, the presence of peaks at higher binding energies (~167–170 eV) can be attributed to oxidized sulfur species, likely formed due to surface oxidation upon air exposure [40, 41]. Notably, the peak assigned to C—S/C═S bonding suggests chemical interaction between the carbon matrix and sulfur species, which can enhance charge transfer and kinetics of Na^+ storage [34]. The N 1s XPS spectra of FeS-NaCl@NC microspheres (Figure 3d) reveal the successful incorporation of nitrogen functionalities within the carbon matrix. The deconvoluted peaks can be assigned to multiple nitrogen configurations, including pyridinic N (398.3 eV), pyrrolic N (399.8 eV), and graphitic N (400.9 eV) [42]. In contrast to FeS-NaCl microspheres, a peak corresponding to graphitic N could be observed in FeS-NaCl@NC microspheres; this suggests partial incorporation of nitrogen into the carbon lattice, which can further improve the electrical conductivity of the composite. The coexistence of these nitrogen species indicates that the polydopamine-derived carbon coating forms a conductive and chemically interactive network. The C 1s spectrum (Figure 3e) shows peaks corresponding to C–C/C═C, C–N/C–S, and N–C═N bonding configurations, further confirming the successful incorporation of nitrogen into the carbon framework [43, 44]. These observations align well with the Raman results (Figures 1i and 2i), which demonstrate that the incorporation of nitrogen leads to an increase in structural disorder (I_D/I_G). The presence of these heteroatom-containing functional groups contributes to improved surface reactivity and charge transfer properties. Thermogravimetric (TG) analysis was conducted to investigate the thermal stability and compositional characteristics of FeS-based microspheres, as shown in Figure 3f. All samples exhibit multiple-step weight loss behavior upon heating. The initial slight weight loss below 200°C can be attributed to the removal of physically adsorbed moisture and residual volatile species. A major weight loss is observed in the temperature range of ~350°C–500°C for all samples, which is mainly associated with the transformation of FeS species into Fe_2O_3 and combustion of dextrin-derived amorphous carbon. Notably, distinct differences are observed among the three samples in the higher temperature region (500°C–650°C). The FeS-NaCl@NC microspheres exhibit a relatively larger weight loss compared to FeS-NaCl and Hollow FeS microspheres, which can be attributed to the oxidation of the N-doped carbon coating derived from polydopamine and graphitic carbon. In contrast, FeS-NaCl and Hollow FeS microspheres show a relatively lower weight loss in this region due to the absence of N-doped carbon coating. Notably, Hollow FeS microspheres exhibit a smaller weight loss in this temperature region in comparison to FeS-NaCl microspheres likely due to their hollow morphology that facilitates faster decomposition and oxidation, and combustion of graphitic carbon may have occurred at a relatively lower temperature. Furthermore, the residual weight at high temperatures (~700°C–800°C) is slightly higher for FeS-NaCl and Hollow FeS microspheres compared to FeS-NaCl@NC microspheres, suggesting that N-doped carbon is completely burned off during heating, resulting in a lower final mass. This is in line with the EA results (Table S1), where FeS-NaCl@NC, FeS-NaCl, and Hollow FeS microspheres exhibit carbon content of 35.1%, 30.2%, and 31.4%, respectively. The porosity characteristics of the samples were analyzed using the Brunauer-Emmett-Teller (BET) analysis. In the N_2 adsorption-desorption isotherm in Figure 3g, FeS-NaCl@NC and FeS-NaCl microspheres exhibit typical type IV isotherms with noticeable hysteresis loops, indicating the presence of mesoporous structures. The specific surface areas of FeS-NaCl@NC, FeS-NaCl, and Hollow FeS microspheres measured via BET method were 113.0, 64.6, and 3.3 $m^2\ g^{-1}$, respectively. Among the samples, FeS-NaCl@NC microspheres show the highest adsorption capacity across the entire pressure range, demonstrating their well-developed porous structure. This enhanced porosity can be attributed to the combined effect of NaCl-derived pores and the N-doped carbon coating. FeS-NaCl microspheres also exhibit a moderate adsorption behavior, confirming that the NaCl-assisted spray pyrolysis and the removal of NaCl particles contribute to the formation of porous structures. In sharp contrast, Hollow FeS microspheres show extremely low nitrogen adsorption over the entire relative pressure range, indicating negligible accessible surface area and pore volume. Despite its hollow morphology, the absence of NaCl templating results in a dense shell structure with limited pore accessibility, behaving as a non-porous material in terms of nitrogen adsorption. The Barrett–Joyner–Halenda (BJH) pore size distribution further supports these observations, as shown in Figure 3h. FeS-NaCl@NC and FeS-NaCl microspheres exhibit a broad size distribution of pores in the range of ~3–200 nm, which indicates the formation of hierarchical pore structure. Meanwhile, Hollow FeS microspheres present nearly flat pore size distribution with minimal pore volume, confirming the lack of developed porous structure.

The electrochemical performance of FeS-NaCl@NC, FeS-NaCl, and Hollow FeS microspheres as anode materials for SIBs was systematically evaluated (Figure 4). Cyclic voltammetry (CV) curves of FeS-NaCl@NC, FeS-NaCl, and Hollow FeS microspheres were recorded at a scan rate of 0.1 mV s^{-1} within the voltage window of 0.001–3.0 V (vs. Na/Na^+), as shown in Figure S8. During the initial cathodic scan, all electrodes exhibit characteristic reduction peaks located at 1.0 V and ~0.2–0.3 V. The peak at ~1.0 V can be attributed to the formation of Na_xFeS accompanied by the decomposition of electrolyte and the formation of a solid electrolyte interphase (SEI) layer [45, 46]. The subsequent broad peak at ~0.2–0.3 V is associated with the conversion reaction of Na_xFeS into metallic Fe and Na_2S [46]. In the anodic scan, an oxidation peak appears at ~1.1–1.2 V, which is attributed to the partial oxidation of Na_2S and the formation of Na_xFeS species [47]. The two anodic peaks above 2.0 V are likely related to the multistep oxidation of reduced Na_xFeS species into intermediate sodium iron sulfides and finally FeS phases [45]. From the second cycle onward, the CV curves of FeS-NaCl@NC and FeS-NaCl microspheres are well overlapped, indicating good reversibility (Figure S8a,b). In contrast, the CV curves of Hollow FeS microspheres exhibit certain degree of deviations from cycle to cycle, suggesting inferior electrochemical reversibility (Figure S8c). The initial charge-discharge profiles of FeS-NaCl@NC, FeS-NaCl, and Hollow FeS microspheres exhibited voltage plateaus, which are in good agreement with the redox behavior observed in the CV curves (Figure 4a–c). The initial charge-discharge profiles of the

16136829, 0, Downloaded from https://onlinelibrary.wiley.com/doi/10.1002/smll.76162 by Massachusetts Institute of Technolo, Wiley Online Library on [08/11/2026]. See the Terms and Conditions (https://onlinelibrary.wiley.com/terms-and-conditions) on Wiley Online Library for rules of use; OA articles are governed by the applicable Creative Commons License

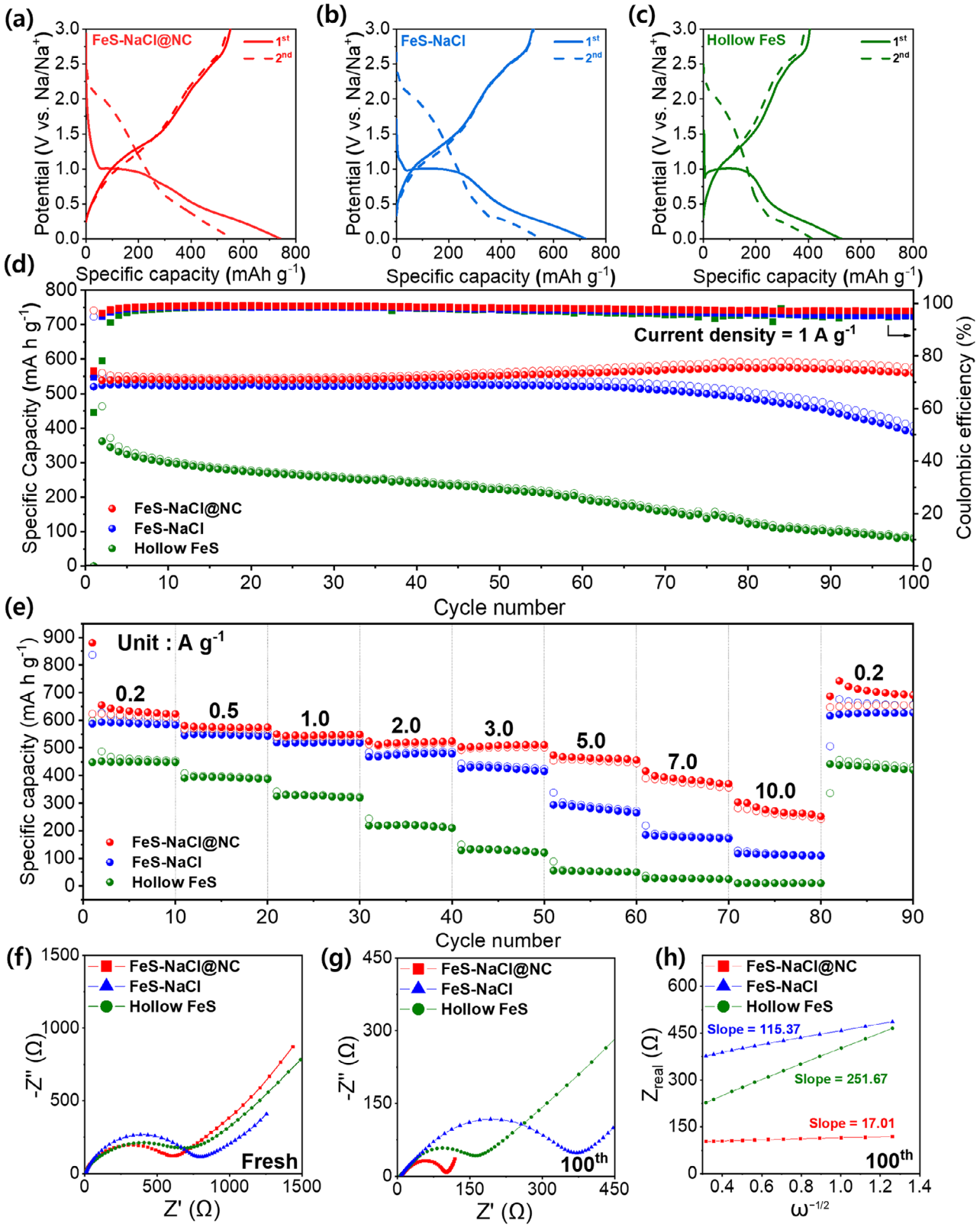


FIGURE 4 | Electrochemical characterization of FeS-NaCl@NC, FeS-NaCl, and Hollow FeS microspheres: (a-c) Charge-discharge profiles of (a) FeS-NaCl@NC, (b) FeS-NaCl, and (c) Hollow FeS microspheres during the initial two cycles. (d) Cycling performance of the microspheres at 1.0 A g^{-1}. (e) Rate capability measured at various current densities. (f,g) Nyquist plots of the microspheres (f) prior to cycling and (g) after 100 cycles. (h) Relationship between Z_{real} vs. $w^{-1/2}$.

16136829, 0, Downloaded from https://onlinelibrary.wiley.com/doi/10.1002/smll.76162 by Massachusetts Institute of Technolo, Wiley Online Library on [08/11/2026]. See the Terms and Conditions (https://onlinelibrary.wiley.com/terms-and-conditions) on Wiley Online Library for rules of use; OA articles are governed by the applicable Creative Commons License

samples exhibit characteristic voltage plateaus associated with the conversion reaction between iron sulfide and Na^+, along with the formation of a SEI. Ex situ XRD and XPS analyses (Figures S9 and S10) further confirmed this conversion behavior. Metallic Fe diffraction peaks and an increased contribution of reduced S^{2-} species were observed after discharge to 0.001 V, supporting the formation of metallic Fe and Na_2S-related species. After charging to 3.0 V, both features were substantially reduced, indicating the reverse conversion toward Fe-sulfide species, although the specific reformation of crystalline Fe_7S_8 could not be unambiguously confirmed due to peak overlap with the Cu current collector. The initial charge/discharge capacities of FeS-NaCl@NC, FeS-NaCl, and Hollow FeS microspheres were 550.2/741.5, 519.9/722.7, and 405.9/526.4 mA h g^{-1}, with initial coulombic efficiency (ICE) of 74.2%, 71.9%, and 77.1%, respectively. FeS-NaCl microspheres exhibit lower ICE in comparison to Hollow FeS microspheres counterparts since they have larger surface area that leads to a higher contact area with the electrolyte, resulting in a higher amount of SEI layer formed on the surface. FeS-NaCl@NC microspheres delivered higher ICEs than the FeS-NaCl microspheres, despite their higher carbon content. This improvement can be attributed to the presence of the N-doped carbon layer, which enhances electrical conductivity and mitigates irreversible side reactions. The long-term cycling performance (Figure 4d) at 1.0 A g^{-1} further highlights the superiority of FeS-NaCl@NC microspheres, where high capacity of 559.6 mA h g^{-1} could be maintained even after 100 cycles. This value is slightly higher than the initial reversible capacity of 550.2 mA h g^{-1}, corresponding to a capacity retention of approximately 101.7%. The modest capacity increase can be reasonably attributed to gradual electrochemical activation during repeated conversion reactions. Progressive electrolyte penetration into the hierarchical pore network, exposure of initially underutilized active sites, and nanoscale reconstruction of conversion-derived Fe/Na_2S domains can increase the number of electrochemically accessible interfaces during cycling. In addition, the reversible formation of a kinetically activated polymer gel-like film on the surface of the active materials, which has been reported for FeS_2-based and other transition-metal compound electrodes, may also partially contribute to the gradual capacity increase [45, 48]. The N-doped carbon coating does not directly provide the additional capacity. Instead, it maintains electrical contact between the reconstructed active domains and suppresses structural and interfacial degradation, thereby allowing the progressively activated sites to contribute reversibly. FeS-NaCl microspheres exhibit high cycling stability until 70th cycle due to the 3D interconnected pore structure that effectively accommodates the volume changes during the repetitive sodiation/desodiation process. However, a gradual capacity decay is observed beyond the 70th cycle for FeS-NaCl microspheres, which clearly demonstrates the critical role of the N-doped carbon coating in enhancing structural stability and maintaining long-term electrochemical performance. Hollow FeS microspheres show significantly lower capacity (~344 mA h g^{-1} for the second cycle) and continuous capacity decay throughout cycling, reaching below ~100 mA h g^{-1} after 100 cycles, indicating poor structural stability and limited electrochemical utilization. This inferior performance can be attributed to the formation of a dense and relatively non-porous shell structure with the absence of NaCl template-derived pore structure, which restricts electrolyte penetration and limits the accessibility of active sites. Furthermore, the hollow shell is prone to structural collapse and pulverization during repeated sodiation/desodiation processes, leading to loss of electrical contact and progressive capacity fading. The coulombic efficiencies of FeS-NaCl@NC and FeS-NaCl microspheres rapidly converge to nearly 99% after the initial cycles, indicating highly reversible sodium storage reactions and the formation of stable electrode/electrolyte interfaces (Figure S11). Notably, FeS-NaCl@NC microspheres exhibit more consistent and stable coulombic efficiency throughout prolonged cycling, which can be attributed to the conformal N-doped carbon coating that effectively suppresses continuous side reactions and stabilizes the SEI layer. To further correlate the excellent long-term cycling performance with the structural stability of the active material, post-cycling TEM analysis was performed on FeS-NaCl@NC microspheres after 100 cycles (Figure S12). The cycled FeS-NaCl@NC microspheres largely retained their three-dimensional porous morphology without severe structural collapse or pulverization (Figure S12a). The higher-magnification TEM image further confirmed the preservation of the porous framework after prolonged cycling (Figure S12b). The SAED pattern (Figure S12c) exhibited predominantly diffuse diffraction features, indicating substantial amorphization of the Fe sulfide phases after repeated conversion reactions. Local structural characteristics were further examined by HR-TEM (Figure S12d) and corresponding fast Fourier transform (FFT) analyses. The FFT pattern obtained from region A showed predominantly diffuse features, confirming its amorphous nature (Figure S12e), whereas distinct diffraction features corresponding to crystalline Fe sulfide phases were observed in region B (Figure S12f), indicating the partial retention of crystalline FeS_2 and Fe_7S_8 domains within the predominantly amorphous matrix. These results demonstrate that prolonged cycling induces substantial amorphization and structural reconstruction of the Fe sulfide phases while locally preserving crystalline Fe sulfide domains. In contrast, Hollow FeS microspheres display relatively fluctuating and delayed stabilization behavior in coulombic efficiency, particularly during the early cycles. This behavior reflects sluggish electrochemical kinetics and unstable interfacial reactions, which originate from the dense shell structure with limited electrolyte accessibility and the absence of a conductive carbon network. The rate capability of the electrodes was evaluated under progressively increasing current densities (Figure 4e). FeS-NaCl@NC microspheres maintain high reversible capacities even at elevated current densities, and their capacity is largely recovered when the current density is returned to a lower value. This behavior indicates excellent structural robustness and fast reaction kinetics. The capacities of FeS-NaCl@NC microspheres were 622.8, 575.0, 548.6, 524.4, 510.8, 455.9, 370.1, and 251.7 mA h g^{-1} at current densities of 0.2, 0.5, 1.0, 2.0, 3.0, 5.0, 7.0, and 10.0 A g^{-1}, respectively. On the other hand, FeS-NaCl microspheres show moderate rate performance with noticeable capacity loss at high current densities, while Hollow FeS microspheres exhibit the poorest rate capability due to their limited ion transport pathways and low electrical conductivity. The superior electrochemical performance of FeS-NaCl@NC microspheres can be attributed to the synergistic combination of NaCl-templated porous architecture and conformal N-doped carbon coating. The interconnected porous network facilitates rapid electrolyte penetration and shortens Na^+ diffusion pathways, while the conductive carbon layer enhances charge transport and stabilizes the electrode structure. Accordingly, the improved rate capability primarily originates from enhanced reaction

16136829, 0, Downloaded from https://onlinelibrary.wiley.com/doi/10.1002/smll.76162 by Massachusetts Institute of Technolo, Wiley Online Library on [08/11/2026]. See the Terms and Conditions (https://onlinelibrary.wiley.com/terms-and-conditions) on Wiley Online Library for rules of use; OA articles are governed by the applicable Creative Commons License

accessibility and reduced electrode-level transport resistance rather than a substantial increase in the intrinsic solid-state Na^+ diffusion coefficient. Also, formation of Fe_7S_8/FeS_2 heterointerfaces at nanoscale has been reported to accelerate the Na^+ ion storage kinetics due to the embedded built-in potential formed between the two different phases [11, 49]. To further verify the beneficial role of the heterointerfaces, phase-controlled Fe_7S_8-NaCl@NC microspheres consisting of only Fe_7S_8 phase were additionally prepared by increasing the amount of thiourea during the sulfidation heat treatment, while retaining the NaCl-templated porous structure and N-doped carbon coating. Compared with the FeS_2/Fe_7S_8 heterostructured FeS-NaCl@NC microspheres, Fe_7S_8-NaCl@NC microspheres exhibited lower reversible capacity and coulombic efficiency as well as inferior rate capability, particularly at high current densities (Figure S13). These results further support the beneficial contribution of FeS_2/Fe_7S_8 heterointerfaces to the enhanced electrochemical performance. Electrochemical impedance spectroscopy (EIS) measurements were conducted to investigate the interfacial charge transfer behavior and ion diffusion kinetics of the FeS-based electrodes. Nyquist plots for FeS-NaCl@NC, Hollow FeS, and FeS-NaCl electrodes were collected at different cycling states, including fresh, first, fifth, 10^{th}, 50^{th}, and 100^{th} cycles (Figure 4f,g and Figure S14). All the Nyquist plots were deconvoluted with the Randles-type equivalent circuit shown in Figure S15. In the fresh state, all electrodes exhibit a depressed semicircle in the high-to-medium frequency region followed by an inclined line in the low-frequency region, corresponding to the charge transfer resistance (R_{ct}) and Warburg impedance associated with Na^+ diffusion, respectively [50]. FeS-NaCl microspheres exhibited higher R_{ct} values than Hollow FeS microspheres, which can be attributed to their 3D porous walls with a larger surface area. FeS-NaCl@NC microspheres show a relatively smaller semicircle compared to FeS-NaCl and Hollow FeS microspheres, indicating reduced interfacial resistance due to the conductive N-doped carbon network. To quantitatively evaluate the evolution of the electrode/electrolyte interface during cycling, the R_{SEI} and R_{ct} values were plotted as functions of cycle number (Figure S16). In the fresh state, only one depressed semicircle was clearly resolved; therefore, the corresponding resistance was assigned to R_{ct}, while R_{SEI} was not separately determined. After the first cycle, R_{ct} markedly decreased for all electrodes, indicating electrochemical activation and improved electrolyte accessibility following the initial conversion reaction. During subsequent cycling, FeS-NaCl@NC maintained substantially lower R_{ct} values than the control electrodes, indicating well-preserved charge-transfer pathways. Similarly, its R_{SEI} remained relatively low and stable, whereas FeS-NaCl and Hollow FeS exhibited more pronounced SEI growth during prolonged cycling. These results demonstrate that the NaCl-derived porous architecture combined with the conductive carbon coating effectively suppresses both R_{SEI} and R_{ct} growth during repeated cycling, thereby maintaining stable electrode/electrolyte interfaces and efficient charge transport. The impedance analysis in the low-frequency region (Figure 4h) reveals the correlation between Z_{re} and $\omega^{-1/2}$ for the prepared microspheres. Notably, the slope of FeS-NaCl@NC microspheres is significantly lower than that of FeS-NaCl and Hollow FeS counterparts after 100 cycles. This indicates that FeS-NaCl@NC microspheres maintain enhanced Na-ion diffusion kinetics even after prolonged cycling, demonstrating their superior structural stability and preserved charge transport pathways [51]. In contrast, the steeper slopes observed for the latter samples after 100 cycles suggest increased diffusion resistance, likely arising from structural degradation and sluggish ion transport during repeated sodiation/desodiation processes. These features collectively enable improved reversibility, cycling stability, and rate capability, demonstrating the effectiveness of the proposed structural design for high-performance sodium-ion battery anodes. To further elucidate the dynamic evolution of interfacial resistance during electrochemical reactions, in situ EIS measurements were performed for FeS-NaCl@NC, FeS-NaCl, and Hollow FeS microspheres, as shown in Figure S17a–c. The Nyquist plots were collected at selected potentials along the charge-discharge profiles, enabling real-time tracking of resistance variation during electrochemical reactions. The total resistance (R_{tot}) was estimated from the combined contribution of SEI resistance (R_{SEI}) and R_{ct}, and its variation as a function of potential was analyzed (Figure S17d–f). For FeS-NaCl@NC microspheres, R_{tot} gradually decreases during the initial sodiation process (down to ~1.0 V), which can be attributed to the formation of a thin ion-conductive SEI layer [52]. As the potential further decreases to ~0.2–0.3 V, corresponding to the conversion reaction of FeS into metallic Fe and Na_2S, R_{tot} shows an additional decrease due to the generation of conductive metallic Fe [52]. A progressive decrease in R_{ct} was observed during the charge process, which is closely related to the volume contraction occurring upon desodiation. For FeS-NaCl@NC microspheres, an abrupt increase in R_{tot} value is observed at 1.5-2.0 V, which is due to the conversion reaction from metallic Fe into Na_xFeS species [53]. This feature is not clearly observed for FeS-NaCl and Hollow FeS microspheres, presumably because their inherently large resistance and sluggish reaction kinetics obscure such localized resistance variation, while the highly conductive and structurally stable N-doped carbon-coated framework enables a more distinct and synchronized phase evolution in FeS-NaCl@NC microspheres. After the transformation of Na_xFeS species back into FeS, R_{tot} values decreased again. FeS-NaCl@NC microspheres exhibit much smaller R_{tot} values in comparison to FeS-NaCl and Hollow FeS microspheres, which clearly demonstrates the role of N-doped carbon coating layer on enhancing Na^+ diffusion, stabilizing the SEI layer, and promoting fast charge transfer kinetics.

To closely elucidate the enhanced structural stability of FeS-NaCl@NC microspheres during cycling, cross-sectional SEM analysis was conducted (Figure 5a–c). In case of FeS-NaCl@NC microspheres, the electrode thickness increased from 37.8 μm in the fresh state to 68.1 μm after the first sodiation, corresponding to a moderate volume expansion of approximately 80.2% (Figure 5d). Upon subsequent desodiation, the thickness decreased to 38.4 μm, showing only a slight residual increase of 1.6% compared to the initial state. The increase in the thickness of FeS-NaCl and Hollow FeS microspheres after 1 full cycle was 2.4% and 49.3% in comparison to the initial state (Figures S18 and S19). The minimal irreversible expansion of FeS-NaCl@NC microspheres indicates that the electrode structure is well preserved during cycling, effectively accommodating the volume change during repetitive cycling. The mechanical characteristics of the FeS-NaCl and Hollow FeS microspheres were further analyzed by nano-indentation to understand the effect of NaCl-derived pores during cycling. The SEM images of the nano-indented electrodes after cycling (Figure 5e,f and Figure S20a,b) confirm that the electrode surfaces remain mechanically intact, enabling

16136829, 0, Downloaded from https://onlinelibrary.wiley.com/doi/10.1002/smll.76162 by Massachusetts Institute of Technolo, Wiley Online Library on [08/11/2026]. See the Terms and Conditions (https://onlinelibrary.wiley.com/terms-and-conditions) on Wiley Online Library for rules of use; OA articles are governed by the applicable Creative Commons License

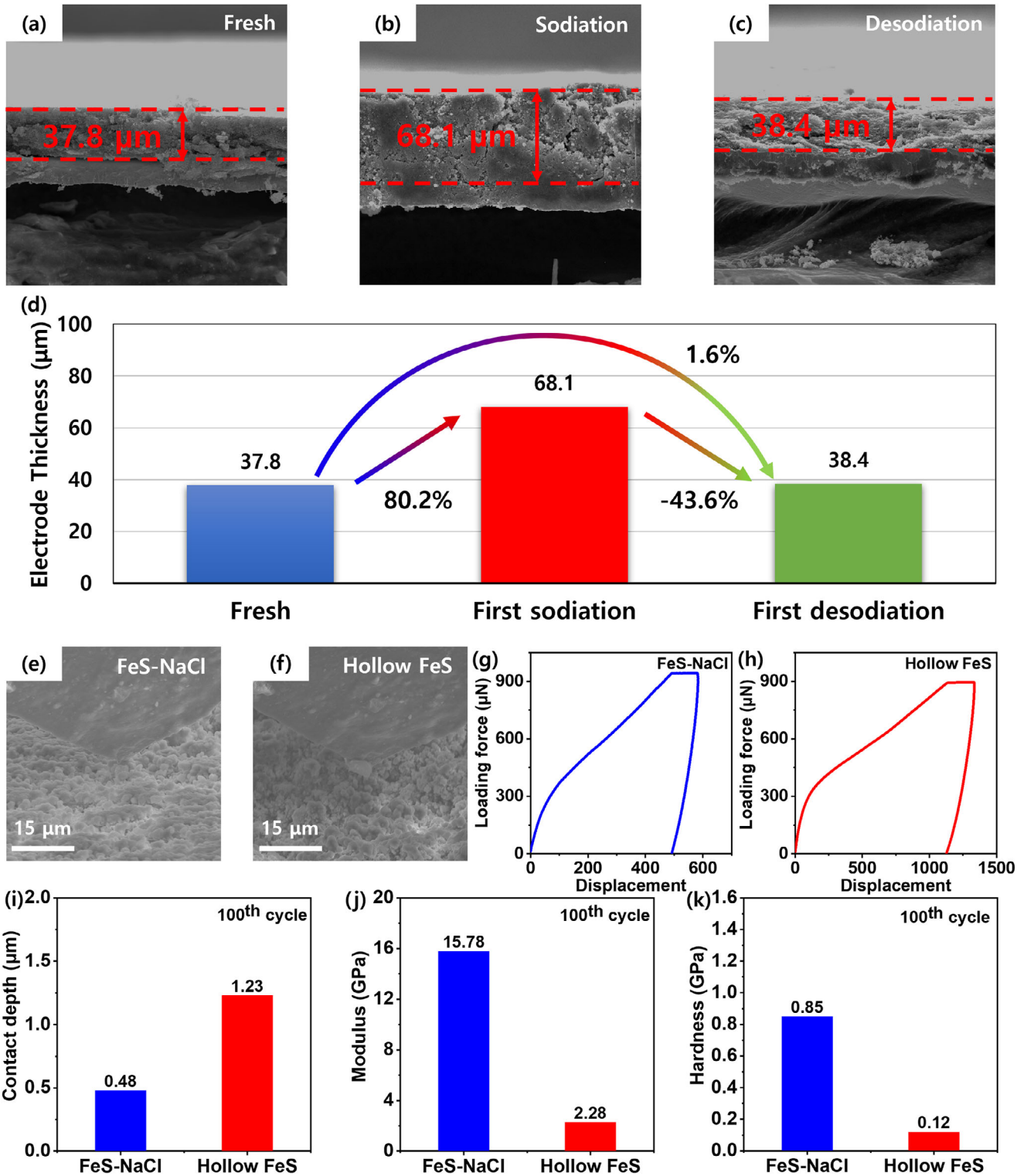


FIGURE 5 | Cross-sectional FE-SEM images of FeS-NaCl@NC microspheres: (a) Prior to cycling, (b) after initial sodiation, (c) after de-sodiation process and (d) electrode swelling rate observed during the initial sodiation/de-sodiation step. (e,f) SEM images from the nano-indentation analysis of FeS-NaCl and Hollow FeS microspheres. (g,h) Loading force–displacement curves, (i) contact depth, (j) modulus (k) hardness of FeS-NaCl and Hollow FeS microspheres after the 100th cycle, highlighting the effect of NaCl-derived pore structures on mechanical stability.

reliable indentation measurements. To evaluate the mechanical response, the electrodes were pressed by an indenter tip, and the corresponding loading force and displacement were recorded (Figure 5g,h and Figure S20c,d). After the second cycle, FeS-NaCl and Hollow FeS electrodes exhibited no distinct trend in mechanical properties despite some differences in absolute values, with contact depths of approximately 1.25 μm for FeS-NaCl and 0.9 μm for Hollow FeS (Figure S20e). Similarly, the modulus was 1.87 GPa for FeS-NaCl and 2.63 GPa for Hollow FeS, while the hardness values were 0.12 GPa and 0.23 GPa, respectively (Figure S20f,g).

16136829, 0, Downloaded from https://onlinelibrary.wiley.com/doi/10.1002/smll.76162 by Massachusetts Institute of Technolo, Wiley Online Library on [08/11/2026]. See the Terms and Conditions (https://onlinelibrary.wiley.com/terms-and-conditions) on Wiley Online Library for rules of use; OA articles are governed by the applicable Creative Commons License

This can be attributed to its denser surface structure with fewer internal pores, which provides greater resistance to deformation under applied stress. In contrast, the FeS-NaCl microspheres, possessing a porous architecture, show relatively lower modulus and hardness at the early stage. However, after prolonged cycling (100th cycle), a pronounced difference emerged. FeS-NaCl electrode showed a significantly lower contact depth (0.48 μm) compared to Hollow FeS (1.23 μm), indicating reduced plastic deformation under applied load (Figure 5i). Correspondingly, the modulus of FeS-NaCl (15.78 GPa) was markedly higher than that of Hollow FeS (2.28 GPa), along with a substantially enhanced hardness of 0.85 GPa for FeS-NaCl compared to 0.12 GPa for Hollow FeS (Figure 5j,k). As a result, FeS-NaCl microspheres exhibit superior resistance to deformation and structural degradation compared to the Hollow FeS counterpart. These findings clearly demonstrate that the NaCl-templated structure plays a crucial role in stabilizing not only the material-level structure but also the electrode-level framework, which is directly correlated with the improved cycling performance.

To quantitatively elucidate the origin of the enhanced rate capability arising from the NaCl-assisted structural design and N-doped carbon coating, CV measurements were conducted for FeS-NaCl@NC, FeS-NaCl, and Hollow FeS microspheres at various scan rates ranging from 0.1 to 3.0 mV s^{-1} within a potential window of 0.001–3.0 V (Figure 6a–c). The electrochemical kinetics of the three samples were analyzed based on the power-law relationship ($i = av^b$), where the *b*-value provides insight into the charge storage mechanism [54]. A *b*-value approaching 1 indicates a dominant surface-controlled (capacitive) process, whereas a value near 0.5 corresponds to diffusion-limited behavior. The calculated *b*-values for FeS-NaCl@NC microspheres at the representative redox peaks were significantly higher (close to unity) than those of FeS-NaCl and Hollow FeS microspheres (Figure 6d–f), indicating that the charge storage process in FeS-NaCl@NC microspheres is predominantly governed by fast surface capacitive reactions. In contrast, Hollow FeS microspheres exhibited relatively lower *b*-values, suggesting sluggish Na^+ diffusion kinetics and a diffusion-controlled reaction mechanism. To further quantify the charge storage contributions, the total current response at a given potential was separated into capacitive (k_1v) and diffusion-controlled ($k_2v^{1/2}$) components using the equation $i = k_1v + k_2v^{1/2}$ [55]. Based on this equation, the capacitive contributions were visualized as shaded regions in the CV curves at various scan rates (Figure 6g–i and Figures S21–S23). FeS-NaCl@NC microspheres exhibited the largest capacitive contribution, accounting for approximately 94% of the total current at 3.0 mV s^{-1}, which is higher than those of FeS-NaCl (92%) and Hollow FeS (57%) microspheres (Figure 6g–i). Figure 6j summarizes the capacitive contribution as a function of scan rate. Even at a low scan rate of 0.1 mV s^{-1}, FeS-NaCl@NC microspheres maintained a high capacitive contribution of 73%, exceeding those of FeS-NaCl and Hollow FeS microspheres. As the scan rate increased, the capacitive contribution of all samples increased; however, FeS-NaCl@NC microspheres consistently exhibited the highest values over the entire scan rate range. Hollow FeS microspheres exhibited a markedly low capacitive contribution, accounting for only ~21% at 0.1 mV s^{-1} and ~57% at 3.0 mV s^{-1}, respectively, clearly highlighting the crucial role of NaCl incorporation in enhancing surface-driven charge storage behavior. The hierarchical porosity induced by NaCl templating facilitates electrolyte penetration and shortens Na^+ diffusion pathways, while the conductive carbon matrix improves electron transport and provides abundant active sites. Consequently, FeS-NaCl@NC microspheres exhibit accelerated electrochemical kinetics and superior rate capability compared to the control samples.

To further elucidate the Na^+ diffusion kinetics of FeS-NaCl@NC, FeS-NaCl, and Hollow FeS microspheres, galvanostatic intermittent titration technique (GITT) measurements were conducted (Figure S24) [56, 57]. The GITT measurements were performed at a current density of 0.1 A g^{-1} using 20 min current pulses followed by 60 min relaxation periods to ensure sufficient voltage equilibration. The Na^+ diffusion coefficient (D_{Na+}) was calculated according to the following equation:

$$D_{Na^+} = \frac{4}{\pi\tau}\left(\frac{m_B V_M}{M_B S}\right)^2\left(\frac{\Delta E_S}{\Delta E_\tau}\right)^2 \quad \left(\tau \ll \frac{L^2}{D_{Na^+}}\right)$$

where τ is the duration of the current pulse, m_B and M_B are the mass and molar mass of the active material, respectively, V_M is the molar volume, and S is the electrode/electrolyte contact area. ΔE_S represents the steady-state voltage change after the relaxation period, whereas ΔE_τ corresponds to the transient voltage change during the current pulse after correcting for the iR drop. The values of the parameters used for the calculation of the Na^+ diffusion coefficient are summarized in Table S3. The GITT voltage profiles (Figure S24a) exhibit typical stepwise responses during both sodiation and desodiation processes, reflecting the transient polarization and subsequent relaxation behavior of the electrode. Based on the GITT analysis, D_{Na+} values were calculated as a function of potential (Figure S24b,c). The three electrodes exhibit D_{Na+} values within a broadly comparable range over most of the sodiation and desodiation processes, although local variations occur at selected potentials. This result indicates that the distinct rate capabilities of the electrodes cannot be primarily attributed to a substantial difference in their intrinsic solid-state Na^+ diffusion coefficients. Instead, the superior rate performance of FeS-NaCl@NC mainly originates from its higher surface-controlled contribution, lower charge-transfer resistance, improved electrolyte accessibility, and preservation of short ion/electron transport pathways. Therefore, the GITT results, together with the CV and EIS analyses, distinguish the comparable intrinsic bulk diffusion behavior from the substantially improved electrode-level reaction kinetics of FeS-NaCl@NC.

To evaluate the practical applicability of the well-controlled FeS-NaCl@NC composite anode, a pouch-type full-cell was fabricated using $NaNi_{0.33}Mn_{0.33}Fe_{0.33}O_2$ as the cathode (N/P electrode capacity ratio of 1.1:1). $NaNi_{0.33}Mn_{0.33}Fe_{0.33}O_2$ was selected as it is one of the promising cathode material candidates for SIBs. As shown in Figure 7a, $NaNi_{0.33}Mn_{0.33}Fe_{0.33}O_2$||FeS-NaCl@NC full-cell was pre-activated at a rate of 0.1 C in the voltage range of 0.8–4.0 V. Although the full-cell exhibited a high initial charge capacity of 153.0 mA h g^{-1}, its initial discharge capacity was approximately 81.2 mA h g^{-1}, resulting in a low ICE of 53.1%. This large initial irreversible capacity is attributed to the low ICE (~74.2%) of FeS-NaCl@NC microspheres and the initial irreversible capacity of $NaNi_{0.33}Mn_{0.33}Fe_{0.33}O_2$. As cycling progresses, the coulombic efficiency of the full-cell steadily improves, ultimately exceeding 99.8% (Figure 7a,c). As shown in the

16136829, 0, Downloaded from https://onlinelibrary.wiley.com/doi/10.1002/smll.76162 by Massachusetts Institute of Technolo, Wiley Online Library on [08/11/2026]. See the Terms and Conditions (https://onlinelibrary.wiley.com/terms-and-conditions) on Wiley Online Library for rules of use; OA articles are governed by the applicable Creative Commons License

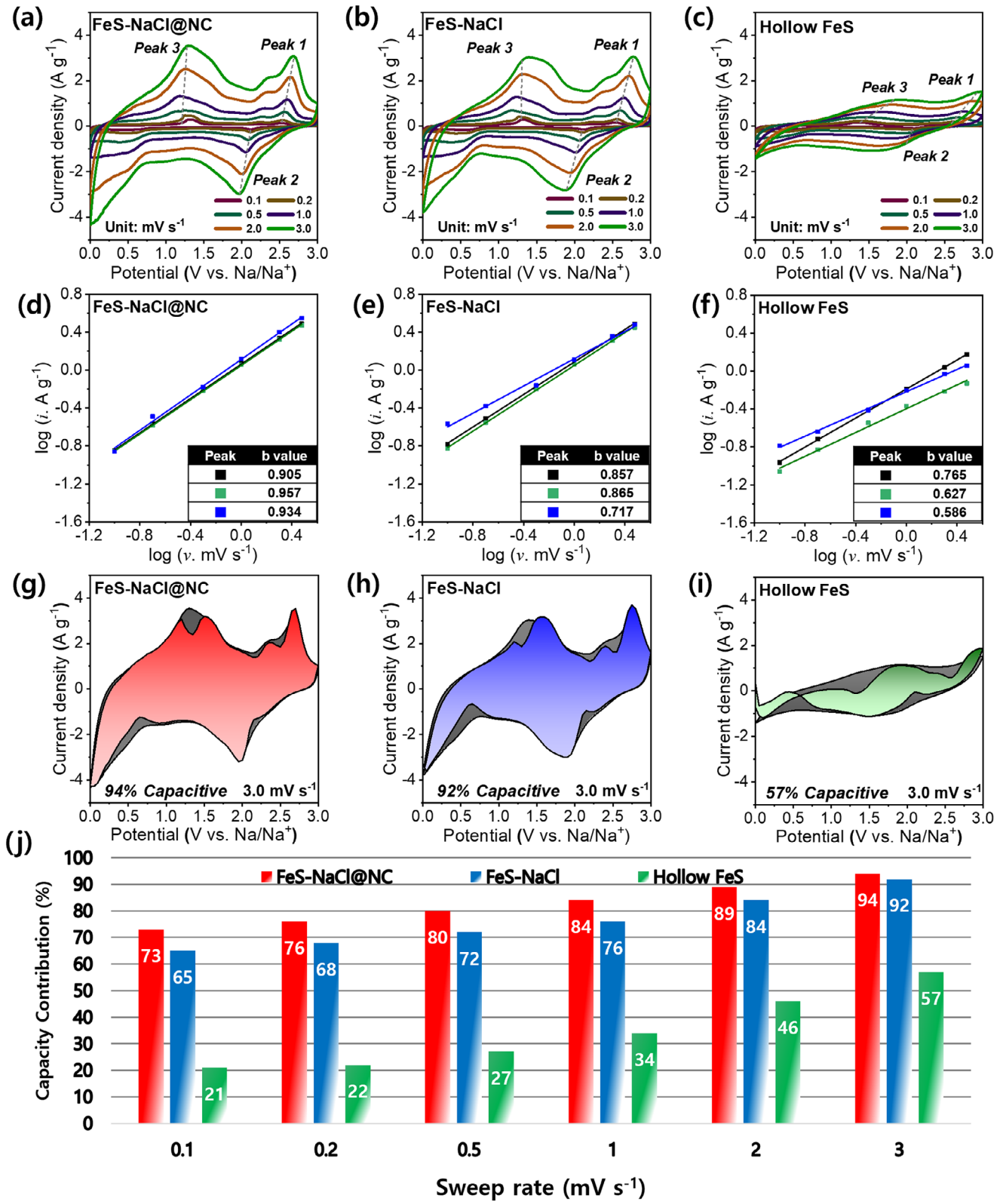


FIGURE 6 | Electrochemical kinetics of the microspheres: (a–c) CV curves measured at various scan rates for (a) FeS-NaCl@NC, (b) FeS-NaCl, and (c) Hollow FeS microspheres. (d–f) Corresponding log *v* vs. log *i* plots with derived *b*-values for both anodic and cathodic peaks. (g–i) Deconvolution of capacitive and diffusion-controlled current contributions at a scan rate of 3 mV s^{-1}, and (j) comparison of the capacitive contribution ratios as a function of scan rate.

16136829, 0, Downloaded from https://onlinelibrary.wiley.com/doi/10.1002/smll.76162 by Massachusetts Institute of Technolo, Wiley Online Library on [08/11/2026]. See the Terms and Conditions (https://onlinelibrary.wiley.com/terms-and-conditions) on Wiley Online Library for rules of use; OA articles are governed by the applicable Creative Commons License

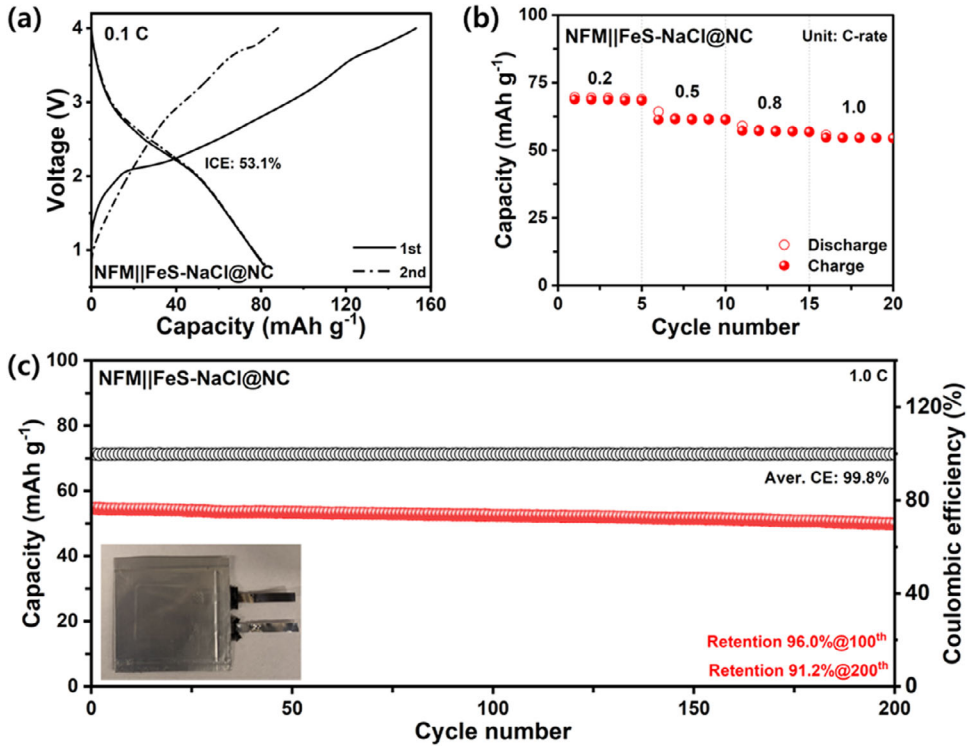


FIGURE 7 | (a) The galvanostatic charge-discharge profiles of the full-cell comprising the FeS-NaCl@NC anode and NFM cathode. (b) Rate performance of the full-cell at various C-rates from 0.2 to 1.0 C (1.0 C = 120 mA g^{-1}). (c) Cycling performance of the full-cell at 1.0 C for 200 cycles (inset NFM||FeS-NaCl@NC full-cell).

rate capability results (Figure 7b), $NaNi_{0.33}Mn_{0.33}Fe_{0.33}O_2$||FeS-NaCl@NC full-cell exhibited capacities of 69.6, 64.3, 59.0, and 55.7 mA h g^{-1} at 0.2, 0.5, 0.8, and 1.0 C, respectively, maintaining a remarkable 80.0% capacity retention at 1.0 C relative to 0.2 C. These results highlight the excellent practical applicability of the fast sodium-ion storage capabilities of FeS-NaCl@NC microspheres, benefiting from their porous framework and N-doped carbon coating layer. Furthermore, the 3D structure and the stable N-doped carbon coating layer on the surface ensure excellent mechanical and chemical stability even in the full-cell application, demonstrating a superior capacity retention of 96.0% after 100 cycles and 91.2% after 200 cycles at 1.0 C. Therefore, FeS-NaCl@NC microspheres developed in this study, which feature a well-designed 3D porous structure and a stable, highly conductive N-doped carbon coating layer, possess excellent practical potential. We expect that it will provide an important guide for the development of advanced SIBs.

3 | Conclusions

In this work, we developed NaCl-derived 3D porous iron sulfide-carbon composite microspheres to which a conformal N-doped carbon layer is coated via a scalable spray pyrolysis process combined with sulfidation heat treatment and polydopamine-derived carbon coating. The NaCl template plays a critical role in constructing a 3D interconnected porous architecture with internal void networks, while the conformal N-doped carbon layer enhances electronic conductivity and interfacial stability. This synergistic structural design enables efficient electrolyte penetration, shortened Na^+ diffusion pathways, and improved charge transfer kinetics. As a result, FeS-NaCl@NC microspheres exhibit significantly enhanced electrochemical performance compared to FeS-NaCl and Hollow FeS microsphere counterparts, delivering superior cycling stability, high rate capability, and stable coulombic efficiency. Nano-indentation and cross-sectional SEM analyses confirm that the NaCl-templated porous framework effectively accommodates volume changes, leading to improved mechanical robustness and structural integrity during prolonged cycling. In addition, kinetic analyses reveal a dominant surface-controlled capacitive behavior and reduced electrode-level transport resistance. Furthermore, the practical applicability of FeS-NaCl@NC microspheres is demonstrated through pouch-type full-cell evaluation with an NFM cathode, showing stable long-term cycling performance with high-capacity retention. Overall, this study provides a scalable and effective strategy for designing high-performance metal sulfide-based anodes for advanced sodium-ion batteries.

4 | Experimental Section

4.1 | Materials

FeS-NaCl@NC microspheres were synthesized via a spray pyrolysis process combined with subsequent sulfidation treatment and polydopamine-derived carbon coating process. Initially, the spray solution was prepared by dissolving 0.1 M iron nitrate nonahydrate ($Fe(NO_3)_3{\cdot}9H_2O$, JUNSEI, 98.0%, $M_w = 404.00$), 30 g L^{-1} dextrin ($(C_6H_{10}O_5)_x{\cdot}nH_2O$, SAMCHUN), and 75 g L^{-1} sodium chloride (NaCl, SAMCHUN, 99.5%) in 500 mL of distilled (DI) water. The solution was vigorously stirred to ensure complete

16136829, 0, Downloaded from https://onlinelibrary.wiley.com/doi/10.1002/smll.76162 by Massachusetts Institute of Technolo, Wiley Online Library on [08/11/2026]. See the Terms and Conditions (https://onlinelibrary.wiley.com/terms-and-conditions) on Wiley Online Library for rules of use; OA articles are governed by the applicable Creative Commons License

dissolution. The prepared solution was then atomized into droplets using an ultrasonic nebulizer, and the droplets were transferred to a quartz reactor, which was heated to 700°C. N_2 gas (10 L min^{-1}) was supplied as the carrier gas to carry the atomized droplets. The powder obtained after the spray pyrolysis was designated as 'Fe_2O_3-NaCl'. Thereafter, Fe_2O_3-NaCl powder was thoroughly washed with deionized water to completely remove the NaCl template, thereby forming the internal empty nanoroom structure.

For the subsequent sulfidation process, a small alumina boat containing the prepared powder was loaded onto a larger alumina boat to which a cover was later put onto. Thiourea was placed in the space between the outer wall of the small boat and the inner wall of the large boat. This nested setup was heat-treated at 200°C for 6 h at a ramping rate of 5°C min^{-1} under a 10% H_2/Ar gas mixture. During the sulfidation process, H_2S gas is generated, which subsequently facilitates the sulfidation reaction. The sample obtained after this sulfidation process was named FeS-NaCl microspheres.

Finally, an N-doped carbon coating layer was introduced to FeS-NaCl microspheres. 0.1214 g of Tris buffer (Sigma 7–9, $NH_2C(CH_2OH)_3$, Sigma–Aldrich, ≥99% (titration)) was dissolved in 100 mL of DI water, followed by the dispersion of 0.1 g of the FeS-NaCl powder. After achieving a homogeneous mixture, 0.025 g of dopamine hydrochloride ($(HO)_2C_6H_3CH_2CH_2NH_2{\cdot}HCl$, Sigma-Aldrich, ≥98%) was added. The solution was continuously stirred for 24 h at room temperature to allow the uniform coating of polydopamine. The resulting powder was washed thoroughly with DI water and dried. To obtain the N-doped carbon-coated sample, designated as FeS-NaCl@NC, the powder was carbonized at 400°C for 3 h with a heating rate of 5°C min^{-1} under an Ar atmosphere.

For comparison, Hollow FeS microspheres were synthesized using the identical procedure, but without NaCl and the N-doped carbon coating. Instead, the NaCl-free precursor was directly sulfidized.

4.2 | Materials Characterization

Surface morphology and elemental distribution were characterized using field emission scanning electron microscopy (FE-SEM; Hitachi S-4800) and field emission transmission electron microscopy (FE-TEM) equipped with energy dispersive x-ray spectroscopy (EDS) (JEOL JM-2100F). Crystallographic properties were analyzed by x-ray diffraction (XRD; X-Pert PRO, Cu K_α radiation) at Korea Basic Science Institute (KBSI) Daegu Center, while the chemical states of FeS-NaCl@NC and FeS-NaCl microspheres were identified via x-ray photoelectron spectroscopy (XPS; Thermo Scientific K-Alpha). To evaluate the carbon content, thermogravimetric analysis (TG; Pyris 1 Thermogravimetric Analyzer, Perkin Elmer) was performed between 25 and 800°C under an air atmosphere. The pore structure of the materials was assessed via the N_2 adsorption using the Brunauer-Emmett-Teller method (TriStar 3000 and 3Flex 3500, Micromeritics). The structural characteristics of carbon were examined using Raman spectroscopy (Jobin Yvon LabRam HR800) equipped with a 632.8 nm He-Ne laser. Lastly, the elemental composition was determined via elemental analysis (vario MICRO cube, Elementar), where the measurements were conducted through high-temperature combustion at 1200–1400°C. Nano-indentation measurements were performed using a PI-85 nanoindenter (Bruker Corporation, USA) integrated with a FE-SEM (Nova Nano SEM, FEI Company, USA) under an argon-filled environment.

4.3 | Electrochemical Characterization

The electrochemical sodium-ion storage properties of FeS-NaCl@NC composite were evaluated using 2032-type coin cells assembled in an argon-filled glovebox (with H_2O and O_2 levels below 0.1 ppm). To prepare the working electrode, a slurry was prepared by homogenizing FeS-NaCl@NC active material, Super P conductive carbon, and sodium carboxymethyl cellulose binder in a weight ratio of 7:2:1 using deionized water. The resulting mixture was cast onto a copper foil current collector and subsequently dried. The electrodes were punched into circular discs with a diameter of 14 mm. For half-cell configurations, sodium metal served as both the counter and reference electrodes, while a microporous polypropylene membrane was employed as the separator. The electrolyte consisted of 1 M $NaClO_4$ dissolved in a mixture of ethylene carbonate and dimethyl carbonate (1:1, v/v), to which 5 wt.% fluoroethylene carbonate was added. Galvanostatic charge–discharge test was carried out within a potential window of 0.001–3.0 V (vs. Na/Na^+) using a battery testing system at various current densities. To investigate the sodium-ion storage kinetics and electrochemical reaction mechanisms, cyclic voltammetry was performed over the same potential range at sweep rates ranging from 0.1 to 3.0 mV s^{-1}. To elucidate the sodium-ion storage mechanisms and kinetic behavior, in situ and ex situ electrochemical impedance spectroscopy analyses were performed over a frequency range of 0.01 Hz–100 kHz. Additionally, the sodium-ion diffusion coefficients (D_{Na+}) were determined through the galvanostatic intermittent titration technique to evaluate the rate of ion transport during the sodiation/desodiation processes.

For full-cell tests, $NaNi_{0.33}Mn_{0.33}Fe_{0.33}O_2$ (NFM) and FeS-NaCl@NC microspheres were used as the cathode and anode, respectively, with a negative-to-positive (N/P) electrode capacity ratio of 1.1:1. To fabricate the cathode, a slurry was prepared by mixing NFM powder, Super P conductive carbon, and polyvinylidene fluoride binder in a weight ratio of 8:1:1 in N-methyl-2-pyrrolidone. The resulting slurry was cast onto an aluminum foil current collector. For the anode, FeS-NaCl@NC powder (80 wt.%), Super P conductive carbon (10 wt.%), and poly(acrylic acid) (10 wt.%) binder were mixed using deionized water and ethanol to prepare a homogeneous slurry, which was then cast onto a copper foil current collector. All electrodes were dried in a vacuum oven at 100°C for 12 h. The pouch-type full-cells were assembled inside an argon-filled glovebox (with H_2O and O_2 levels below 0.1 ppm). The separator and electrolyte used here were Al_2O_3-coated polyethylene and 0.73 m NaFSI in a mixed solvent of N,N-dimethyl fluorosulfonamide (DMFSA) and N,N-dimethyltrifluoromethanesulfonamide (DMTMSA) (2:1, molar ratio), respectively. The full-cells were activated in the range of 0.8–4.0 V at 0.1 C (1.0 C = 120 mA g^{-1}) using a battery testing system. The rate capability and cycling performance tests were conducted at various C-rates (0.2, 0.5, 0.8, and 1.0 C), and at

16136829, 0, Downloaded from https://onlinelibrary.wiley.com/doi/10.1002/smll.76162 by Massachusetts Institute of Technolo, Wiley Online Library on [08/11/2026]. See the Terms and Conditions (https://onlinelibrary.wiley.com/terms-and-conditions) on Wiley Online Library for rules of use; OA articles are governed by the applicable Creative Commons License

1.0 C, respectively, with a potential window ranging from 0.8 to 3.8 V. Additionally, all the pouch-cells were tested with a uniaxial pressure of ~300 kPa.

Author Contributions

Hyojun Lim: conceptualization, investigation, Writing – original draft, methodology, validation, visualization, formal analysis, data curation. **Yun Chan Kang**: conceptualization, writing – original draft, writing – review and editing, project administration, supervision, resources, investigation, validation. **Ji Myeon Park**: conceptualization, investigation, writing – original draft, methodology, validation, visualization, formal analysis, data curation. **Ju Young Kim**: methodology, investigation, writing – original draft, visualization, validation, formal analysis, data curation. **Jin Hyeong Lee**: investigation, validation, methodology, formal analysis, data curation. **Hwa Young Choi**: investigation, validation, methodology, data curation. **Weiyin Chen**: data curation, formal analysis, visualization, validation, investigation. **Ju Li**: conceptualization, investigation, writing – original draft, validation, writing – review and editing, project administration, resources, supervision. **Jin-Sung Park**: conceptualization, investigation, writing – original draft, validation, writing – review and editing, project administration, supervision, resources. **Jaekyung Sung**: investigation, methodology, validation, data curation. **Seul Jeong**: investigation, methodology, validation, data curation.

Acknowledgements

J.M.P., H.L., and J.Y.K. contributed equally to this work. This research was supported by the Learning & Academic Research Institution for Master's and PhD students, and Postdocs (LAMP) Program of the National Research Foundation of Korea (NRF) grant funded by the Ministry of Education (No. RS-2023-00285390 and No. RS-2023-00301974). This work was supported by the National Research Foundation of Korea (NRF) grant funded by the Korean government (MSIT) (RS-2025-24533849). This work was supported by the Ajou University research fund.

Conflicts of Interest

The authors declare no conflicts of interest.

Data Availability Statement

The data that support the findings of this study are available from the corresponding author upon reasonable request.

References

1. C. Yang, S. Xin, L. Mai, and Y. You, "Materials Design for High-Safety Sodium-Ion Battery," *Advanced Energy Materials* 11 (2021): 2000974, https://doi.org/10.1002/aenm.202000974.

2. C. Vaalma, D. Buchholz, M. Weil, and S. Passerini, "A Cost and Resource Analysis of Sodium-ion Batteries," *Nature Reviews Materials* 3 (2018): 18013, https://doi.org/10.1038/natrevmats.2018.13.

3. J. W. Choi and D. Aurbach, "Promise and Reality of Post-lithium-ion Batteries With High Energy Densities," *Nature Reviews Materials* 1 (2016): 16013, https://doi.org/10.1038/natrevmats.2016.13.

4. J. Deng, W. B. Luo, S. L. Chou, H. K. Liu, and S. X. Dou, "Sodium-Ion Batteries: From Academic Research to Practical Commercialization," *Advanced Energy Materials* 8 (2018): 1701428, https://doi.org/10.1002/aenm.201701428.

5. T. Hosaka, K. Kubota, A. S. Hameed, and S. Komaba, "Research Development on K-Ion Batteries," *Chemical Reviews* 120 (2020): 6358–6466, https://doi.org/10.1021/acs.chemrev.9b00463.

6. M. Sawicki and L. L. Shaw, "Advances and Challenges of Sodium Ion Batteries as Post Lithium Ion Batteries," *RSC Advances* 5 (2015): 53129–53154, https://doi.org/10.1039/C5RA08321D.

7. F. Pan, Z. Li, S. Yao, et al., "Combined Intercalation and Space-charge Mechanism Enabled High-capacity, Ultrafast and Long-lifespan Sodium-ion Storage for Chalcogenide Anodes," *Energy & Environmental Science* 18 (2025): 1856–1866, https://doi.org/10.1039/D4EE03217A.

8. J. S. Park and Y. C. Kang, "Multicomponent (Mo, Ni) Metal Sulfide and Selenide Microspheres With Empty Nanovoids as Anode Materials for Na-ion Batteries," *Journal of Materials Chemistry A* 5 (2017): 8616–8623, https://doi.org/10.1039/C7TA01088E.

9. S. Dai, L. Wang, M. Cao, Z. Zhong, Y. Shen, and M. Wang, "Design Strategies in Metal Chalcogenides Anode Materials for High-Performance Sodium-Ion Battery," *Materials Today Energy* 12 (2019): 114–128, https://doi.org/10.1016/j.mtener.2018.12.011.

10. S. Qiao, Q. Zhou, M. Ma, H. K. Liu, S. X. Dou, and S. Chong, "Advanced Anode Materials for Rechargeable Sodium-Ion Batteries," *ACS Nano* 17 (2023): 11220–11252, https://doi.org/10.1021/acsnano.3c02892.

11. G. D. Park, J. S. Park, J. K. Kim, and Y. C. Kang, "Recent Advances in Heterostructured Anode Materials With Multiple Anions for Advanced Alkali-Ion Batteries," *Advanced Energy Materials* 11 (2021): 2003058, https://doi.org/10.1002/aenm.202003058.

12. J. S. Lee, J. Y. Kim, H. S. Ahn, et al., "Rational Design Strategy of Multicomponent Si/FeSeO x @N-Doped Graphitic Carbon Hybrid Microspheres Intertwined With N-Doped Carbon Nanotubes as Anodes for Ultra-Stable Lithium-Ion Batteries," *Small Structures* 6 (2025): 2400354, https://doi.org/10.1002/sstr.202400354.

13. J. Chen, R. Cao, Z. Li, et al., "Unlocking the Positive Role of Large Volume Expansion in Influencing the Sodium-storage Performance for Transition-metal Selenide Anode," *Energy Storage Materials* 84 (2026): 104794, https://doi.org/10.1016/j.ensm.2025.104794.

14. Y. Jiang, M. Xie, F. Wu, et al., "Cobalt Selenide Hollow Polyhedron Encapsulated in Graphene for High-Performance Lithium/Sodium Storage," *Small* 17 (2021): 2102893, https://doi.org/10.1002/smll.202102893.

15. X. Yang, J. Zhang, Z. Wang, et al., "Carbon-Supported Nickel Selenide Hollow Nanowires as Advanced Anode Materials for Sodium-Ion Batteries," *Small* 14 (2018): 1702669.

16. H. Y. Seo, J. H. Choi, Y. B. Kim, J. S. Cho, Y. C. Kang, and G. D. Park, "Tailoring the Shell Thickness of Yolk–Shell Structured Carbon Microspheres: Applications in Metal Selenide and Carbon Composite Microspheres for Enhanced Sodium Ion Storage Properties," *Journal of Materials Chemistry A* 11 (2023): 24738–24753, https://doi.org/10.1039/D3TA04705A.

17. X. Yang, S. Wang, D. Y. W. Yu, and A. L. Rogach, "Direct Conversion of Metal-organic Frameworks Into Selenium/Selenide/Carbon Composites With High Sodium Storage Capacity," *Nano Energy* 58 (2019): 392–398, https://doi.org/10.1016/j.nanoen.2019.01.064.

18. Z. Ali, M. Asif, X. Huang, T. Tang, and Y. Hou, "Hierarchically Porous Fe_2 $CoSe_4$ Binary-Metal Selenide for Extraordinary Rate Performance and Durable Anode of Sodium-Ion Batteries," *Advanced Materials* 30 (2018): 1802745, https://doi.org/10.1002/adma.201802745.

19. C. Qian, B. Xie, R. Wang, et al., "Heterogeneous Double-layer Mesoporous Hollow Spheres $SnSe_2$@N, Se-C as Anode for Enhanced Energy Storage Performance of Lithium/Sodium Ion Batteries," *Colloids and Surfaces A: Physicochemical and Engineering Aspects* 709 (2025): 136158, https://doi.org/10.1016/j.colsurfa.2025.136158.

20. Y. Zhou, Z. Yao, H. Yang, et al., "Hierarchical MoS_2 Nanosheets Anchored on SnS_2-encapsulated Hollow Carbon Nanofibers as High-performance Anodes for Sodium-ion Batteries," *Journal of Alloys and Compounds* 1056 (2026): 186584, https://doi.org/10.1016/j.jallcom.2026.186584.

21. X. Zhang, Z. Yao, H. Zhang, et al., "Synergistic Selenide Solid Solutions Confined in Pomelo-Templated 3D Carbon Architectures: A Dual-Strategy Design for Ultrastable High-rate Sodium-ion Batteries,"

16136829, 0, Downloaded from https://onlinelibrary.wiley.com/doi/10.1002/smll.76162 by Massachusetts Institute of Technolo, Wiley Online Library on [08/11/2026]. See the Terms and Conditions (https://onlinelibrary.wiley.com/terms-and-conditions) on Wiley Online Library for rules of use; OA articles are governed by the applicable Creative Commons License

Chemical Engineering Journal 520 (2025): 165773, https://doi.org/10.1016/j.cej.2025.165773.

22. Y. Zhou, Z. Yao, H. Zhang, et al., "SnS_2/NiS_2 Heterostructure Confined in N-doped Hollow Carbon Nanofibers as High-rate Anode for Sodium-ion Batteries," *Journal of Colloid and Interface Science* 694 (2025): 137699, https://doi.org/10.1016/j.jcis.2025.137699.

23. Z. Huang, J. Liu, K. Xu, et al., "Structural and Vacancy Assisted Engineering of Cobalt Selenide for Ultrahigh Energy Density Sodium Ion Pouch Cell," *Inorganic Chemistry Frontiers* 11 (2024): 6564–6576, https://doi.org/10.1039/D4QI01573H.

24. J. S. Park, J. K. Kim, J. H. Hong, J. S. Cho, S. K. Park, and Y. C. Kang, "Advances in the Synthesis and Design of Nanostructured Materials by Aerosol Spray Processes for Efficient Energy Storage," *Nanoscale* 11 (2019): 19012–19057, https://doi.org/10.1039/C9NR05575D.

25. A. G. Nguyen, H. T. T. Le, R. Verma, D. L. Vu, and C. J. Park, "Boosting Sodium-ion Battery Performance Using an Antimony Nanoparticle Self-embedded in a 3D Nitrogen-doped Carbon Framework Anode," *Chemical Engineering Journal* 429 (2022): 132359, https://doi.org/10.1016/j.cej.2021.132359.

26. T. Li, H. Dong, Z. Shi, et al., "FeS_2 Nanoparticle/Graphene Composites for Lithium-Ion Storage With S-Vacancy-Induced Enhanced Anode Performances," *ACS Applied Nano Materials* 5 (2022): 8835–8845, https://doi.org/10.1021/acsanm.2c00881.

27. Y. Lu, W. Yu, S. Liu, and L. Zhou, "FeS_2 Anchored to Nitrogen-doped Porous Carbon Nanosheets for Lithium-Sulfur Batteries," *Ionics* 31 (2025): 4195–4208, https://doi.org/10.1007/s11581-025-06257-6.

28. A. Gomez-Martin, J. Martinez-Fernandez, M. Ruttert, et al., "Iron-Catalyzed Graphitic Carbon Materials From Biomass Resources as Anodes for Lithium-Ion Batteries," *Chemsuschem* 11 (2018): 2776–2787, https://doi.org/10.1002/cssc.201800831.

29. C. Lei, F. Han, D. Li, et al., "Dopamine as the Coating Agent and Carbon Precursor for the Fabrication of N-doped Carbon Coated Fe_3O_4 Composites as Superior Lithium Ion Anodes," *Nanoscale* 5 (2013): 1168, https://doi.org/10.1039/c2nr33043a.

30. F. Yang, Z. Zhang, K. Du, et al., "Dopamine Derived Nitrogen-doped Carbon Sheets as Anode Materials for High-performance Sodium Ion Batteries," *Carbon* 91 (2015): 88–95, https://doi.org/10.1016/j.carbon.2015.04.049.

31. F. Wang, S. Lin, X. Lu, R. Hong, and H. Liu, "Poly-dopamine Carbon-coated Stable Silicon/Graphene/CNT Composite as Anode for Lithium Ion Batteries," *Electrochimica Acta* 404 (2022): 139708, https://doi.org/10.1016/j.electacta.2021.139708.

32. T. González-Carreño, M. P. Morales, M. Gracia, and C. J. Serna, "Preparation of Uniform γ-Fe_2O_3 Particles With Nanometer Size by Spray Pyrolysis," *Materials Letters* 18 (1993): 151–155, https://doi.org/10.1016/0167-577X(93)90116-F.

33. R. D. Hunter, J. Ramírez-Rico, and Z. Schnepp, "Iron-catalyzed Graphitization for the Synthesis of Nanostructured Graphitic Carbons," *Journal of Materials Chemistry A* 10 (2022): 4489–4516, https://doi.org/10.1039/D1TA09654K.

34. X. Zhou, Z. Wang, Y. Wang, et al., "Graphene Supported FeS_2 Nanoparticles With Sandwich Structure as a Promising Anode for High-Rate Potassium-Ion Batteries," *Journal of Colloid and Interface Science* 636 (2023): 73–82, https://doi.org/10.1016/j.jcis.2022.12.168.

35. S. Zhao, S. Guo, C. Zhu, et al., "Achieving Electroreduction of CO_2 to CH_3 OH With High Selectivity Using A Pyrite–Nickel Sulfide Nanocomposite," *RSC Advances* 7 (2017): 1376–1381, https://doi.org/10.1039/C6RA26868D.

36. N. Wang, Y. Wang, Z. Lu, R. Cheng, L. Yang, and Y. Li, "Hierarchical Core-shell FeS_2/Fe_7S_8@C Microspheres Embedded Into Interconnected Graphene Framework for High-efficiency Microwave Attenuation," *Carbon* 202 (2023): 254–264, https://doi.org/10.1016/j.carbon.2022.10.083.

37. T. Wang, W. Lv, D. Meng, Q. Liu, Z. Rong, and H. Qiu, "A Novelty Strategy for Preparing Ternary FeS_2-Fe_7S_8-$FeCl_2$ Composite as Anode Materials for Sodium-Ion Batteries," *Journal of Alloys and Compounds* 925 (2022): 166810, https://doi.org/10.1016/j.jallcom.2022.166810.

38. E. N. Primo, M. V. Bracamonte, G. L. Luque, P. G. Bercoff, E. P. M. Leiva, and D. E. Barraco, "Mechanochemically Synthesized Pyrite and Its Electrochemical Behavior as Cathode for Lithium Batteries," *Journal of Solid State Electrochemistry* 23 (2019): 1929–1938, https://doi.org/10.1007/s10008-019-04294-6.

39. H. Liu, Y. Li, G. Lv, X. Liu, and L. Liao, "High-purity Monoclinic Pyrrhotite Derived From Natural Pyrite With Excellent Removal Performance for Cr (VI) and Its Mechanism," *Environmental Science and Pollution Research* 31 (2024): 20234–20245, https://doi.org/10.1007/s11356-024-32445-4.

40. M. Yang, Z. Jin, C. Wang, et al., "Fe Foam-Supported FeS_2–MoS_2 Electrocatalyst for N 2 Reduction Under Ambient Conditions," *ACS Applied Materials & Interfaces* 13 (2021): 55040–55050, https://doi.org/10.1021/acsami.1c16284.

41. Q. Huang, W. Su, G. Zhong, K. Xu, and C. Yang, "Bimetal Heterostructure $NiCo_2Se_4$ Anode Confined by Carbon Nano Boxes for Ultrafast and Stable Potassium Storage," *Chemical Engineering Journal* 460 (2023): 141875, https://doi.org/10.1016/j.cej.2023.141875.

42. D. Y. Osadchii, A. I. Olivos-Suarez, A. V. Bavykina, and J. Gascon, "Revisiting Nitrogen Species in Covalent Triazine Frameworks," *Langmuir* 33 (2017): 14278–14285, https://doi.org/10.1021/acs.langmuir.7b02929.

43. A. K. Haridas, H. Kim, C. H. Choi, H. J. Ahn, and J. H. Ahn, "Simple Design of an In Situ Generated Iron Sulfide/Carbon Heterostructure With N, S Codoping for High Performance Lithium/Sodium-ion Batteries," *Applied Surface Science* 554 (2021): 149587, https://doi.org/10.1016/j.apsusc.2021.149587.

44. R. R. Solís, M. A. Quintana, G. Blázquez, M. Calero, and M. J. Muñoz-Batista, "Ruthenium Deposited Onto Graphitic Carbon Modified With Boron for the Intensified Photocatalytic Production of Benzaldehyde," *Catalysis Today* 423 (2023): 114266.

45. J. S. Cho, J. S. Park, and Y. C. Kang, "Porous FeS Nanofibers With Numerous Nanovoids Obtained by Kirkendall Diffusion Effect for Use as Anode Materials for Sodium-ion Batteries," *Nano Research* 10 (2017): 897–907, https://doi.org/10.1007/s12274-016-1346-9.

46. M. Walter, T. Zünd, and M. V. Kovalenko, "Pyrite (FeS_2) Nanocrystals as Inexpensive High-performance Lithium-ion Cathode and Sodium-ion Anode Materials," *Nanoscale* 7 (2015): 9158–9163, https://doi.org/10.1039/C5NR00398A.

47. X. Huang, Q. He, J. Xun, et al., "Constructing Strain-alleviated Structures in Ultrathin FeS/C Composites for Durable Lithium and Sodium Storage," *Science China Materials* 66 (2023): 2601–2612, https://doi.org/10.1007/s40843-022-2435-3.

48. Z. Zhao, Z. Hu, R. Jiao, et al., "Tailoring Multi-layer Architectured FeS_2@C Hybrids for Superior Sodium-, Potassium- and Aluminum-ion Storage," *Energy Storage Materials* 22 (2019): 228–234, https://doi.org/10.1016/j.ensm.2019.01.022.

49. J. Yin, Q. Zhang, Q. Zhang, et al., "Fe_7S_8/FeS_2 Heterostructures in Carbon Nanospheres for High-Performance Sodium Storage," *ACS Applied Nano Materials* 8 (2025): 6886–6896, https://doi.org/10.1021/acsanm.4c06670.

50. M. Xu, Q. Xia, J. Yue, et al., "Rambutan-Like Hybrid Hollow Spheres of Carbon Confined Co_3O_4 Nanoparticles as Advanced Anode Materials for Sodium-Ion Batteries," *Advanced Functional Materials* 29 (2019): 1807377, https://doi.org/10.1002/adfm.201807377.

51. D. Yang, W. Chen, X. Zhang, et al., "Facile and Scalable Synthesis of Low-cost FeS@C as Long-cycle Anodes for Sodium-ion Batteries," *Journal of Materials Chemistry A* 7 (2019): 19709–19718, https://doi.org/10.1039/C9TA05664E.

16136829, 0, Downloaded from https://onlinelibrary.wiley.com/doi/10.1002/smll.76162 by Massachusetts Institute of Technolo, Wiley Online Library on [08/11/2026]. See the Terms and Conditions (https://onlinelibrary.wiley.com/terms-and-conditions) on Wiley Online Library for rules of use; OA articles are governed by the applicable Creative Commons License

52. M. Han, J. Liu, and C. Deng, "Yolk-Shell Structure and Spin-Polarized Surface Capacitance Enable FeS Stable and Fast Ion Transport in Sodium-Ion Batteries," *Advanced Energy Materials* 14 (2024): 2400246.

53. Y. B. Kim, H. Y. Seo, K. H. Kim, J. S. Cho, Y. C. Kang, and G. D. Park, "Synthesis of Iron Sulfide Nanocrystals Encapsulated in Highly Porous Carbon-Coated CNT Microsphere as Anode Materials for Sodium-Ion Batteries," *Small* 20 (2024): 2305686.

54. H. Zhang, C. Zhu, Y. Lu, et al., "Co-Construction of Selenium Vacancy and Heterogeneous Structure in $FeSe_2$/$NiSe_2$ to Induce Fast Ion Diffusion Kinetics for Potassium-Ion Batteries," *Small* 21 (2025): 07672.

55. Y. Luo, H. He, P. Li, Y. Cai, and M. Zhang, "Graphene-controlled FeSe Nanoparticles Embedded in Carbon Nanofibers for High-Performance Potassium-Ion Batteries," *Science China Materials* 65 (2022): 1751–1760, https://doi.org/10.1007/s40843-021-1969-8.

56. Y. Xu, Y. Zhu, Y. Liu, and C. Wang, "Electrochemical Performance of Porous Carbon/Tin Composite Anodes for Sodium-Ion and Lithium-Ion Batteries," *Advanced Energy Materials* 3 (2013): 128–133, https://doi.org/10.1002/aenm.201200346.

57. Y. B. Kim, T. H. Kim, S. Kim, et al., "Multiple Heteroatom-doped Cobalt Sulfoselenide@C Yolk-shell Microsphere as Excellent Anode Materials for Sodium-ion Batteries and Their Conversion Reaction Mechanism With Sodium Ions," *Journal of Power Sources* 618 (2024): 235186, https://doi.org/10.1016/j.jpowsour.2024.235186.

Supporting Information

Additional supporting information can be found online in the Supporting Information section.

Supporting File: smll76162-sup-0001-SuppMat.docx.

16136829, 0, Downloaded from https://onlinelibrary.wiley.com/doi/10.1002/smll.76162 by Massachusetts Institute of Technolo, Wiley Online Library on [08/11/2026]. See the Terms and Conditions (https://onlinelibrary.wiley.com/terms-and-conditions) on Wiley Online Library for rules of use; OA articles are governed by the applicable Creative Commons License

Supporting Information

NaCl-Templated Iron Sulfide/N-Doped Carbon Microspheres for High-Performance Sodium-Ion Batteries: From Nanostructural Design to Pouch Cells

Ji Myeon Park, Hyojun Lim, Ju Young Kim, Weiyin Chen, Jin Hyeong Lee, Seul Jeong, Hwa Young Choi, Jaekyung Sung, Yun Chan Kang, Ju Li*, Jin-Sung Park**

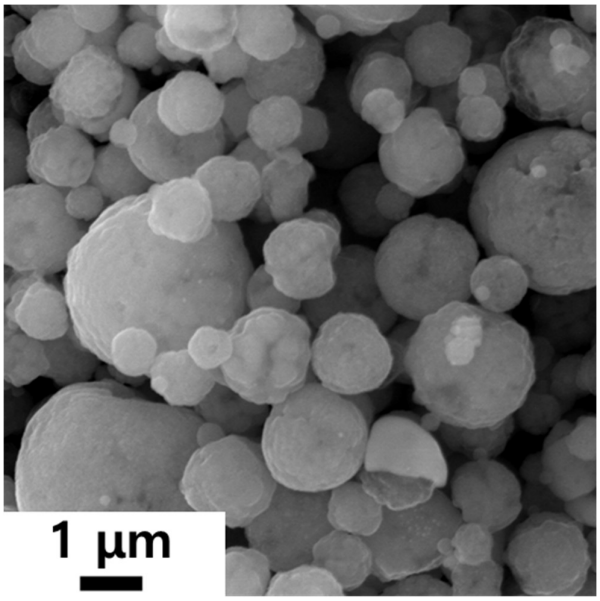


Figure S1. SEM image showing multiple Fe_2O_3-NaCl microspheres prepared directly from spray pyrolysis.

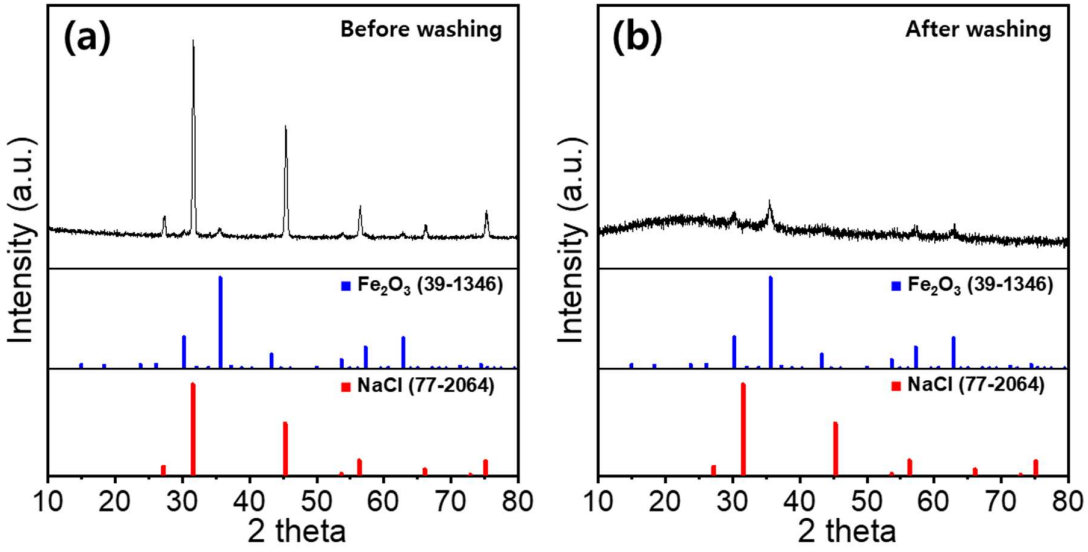
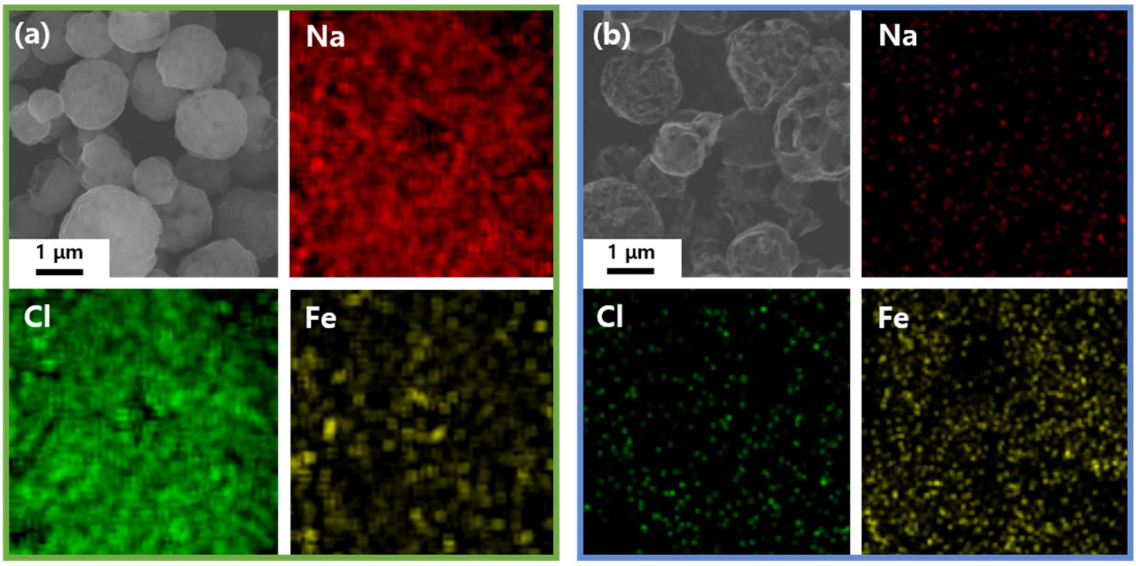


Figure S2. XRD pattern of Fe_2O_3-NaCl microspheres (a) before and (b) after washing.



(c)

Before washing		
Element	**Mass%**	**Atom%**
Na	13.46 ± 0.04	8.71 ± 0.02
Cl	13.50 ± 0.03	5.67 ± 0.01
Fe	2.16 ± 0.02	0.58 ± 0.01
C	62.10 ± 0.10	76.89 ± 0.12
O	8.77 ± 0.06	8.16 ± 0.06
Total	100.00	100.00

(d)

After washing		
Element	**Mass%**	**Atom%**
Na	0.00 ± 0.01	0.00 ± 0.01
Cl	0.00 ± 0.01	0.00 ± 0.00
Fe	2.86 ± 0.03	0.66 ± 0.01
C	76.73 ± 0.07	82.80 ± 0.07
O	20.40 ± 0.13	16.53 ± 0.10
Total	100.00	100.00

Figure S3. SEM images and corresponding elemental dot mapping images of Fe_2O_3-NaCl microspheres (a) before and (b) after washing with deionized water, and the corresponding quantitative EDS results (c) before and (d) after washing.

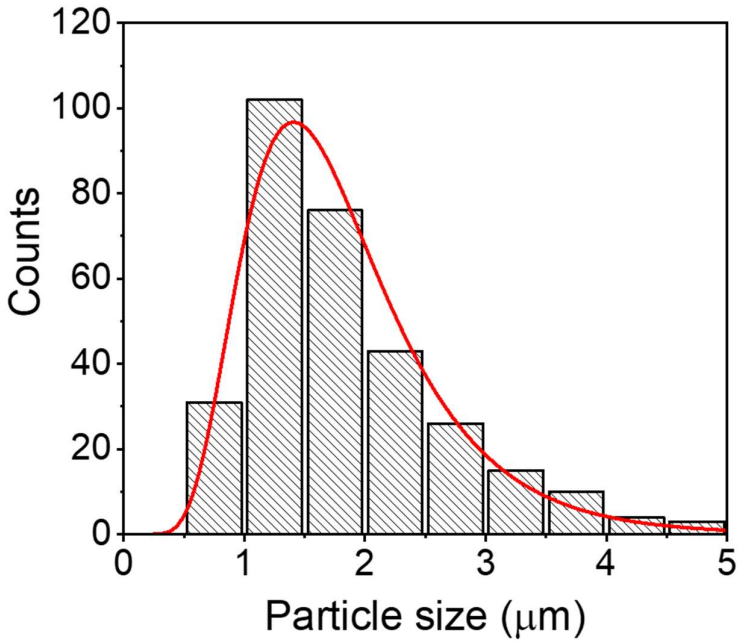


Figure S4. Size distribution of FeS-NaCl@NC microspheres.

Sample	N[%]	C[%]	H[%]	S[%]
FeS-NaCl@NC	5.559	35.115	0.36	25.766
FeS-NaCl	12.965	30.239	0.818	26.648
Hollow FeS	12.537	31.35	1.249	27.801

Table S1. EA results of FeS-NaCl@NC, FeS-NaCl, and Hollow FeS microspheres.

FeS-NaCl	Before Washing		After washing	
Element	Mass%	Atom%	Mass%	Atom%
C	67.57±0.06	84.65±0.08	92.54±0.07	97.79±0.08
N	5.22±0.16	5.61±0.17	N/A	N/A
S	12.06±0.02	5.66±0.01	3.07±0.02	1.22±0.01
Fe	15.15±0.04	4.08±0.01	4.39±0.04	1.00±0.01
Total	100.00	100.00	100.00	100.00

Table S2. EDS analysis results of FeS-NaCl microspheres before and after DI-water washing.

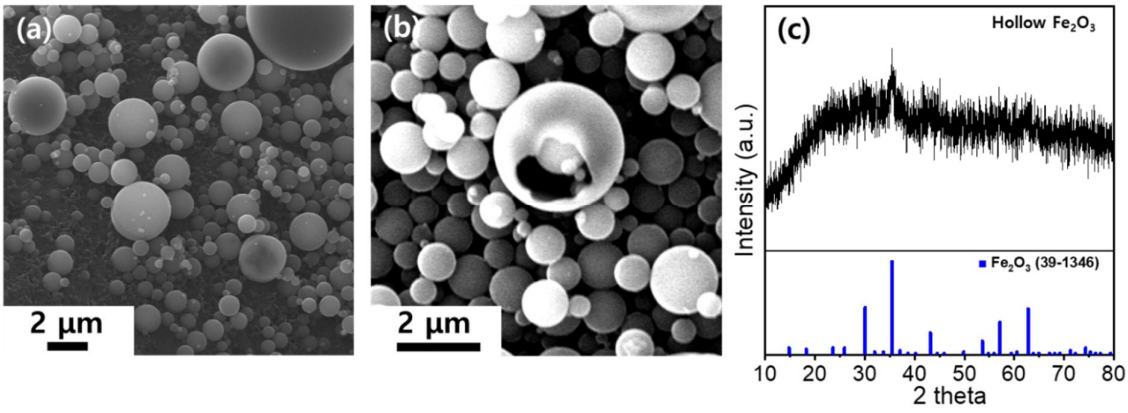


Figure S5. (a,b) SEM images and (c) XRD pattern of Hollow Fe_2O_3 microspheres.

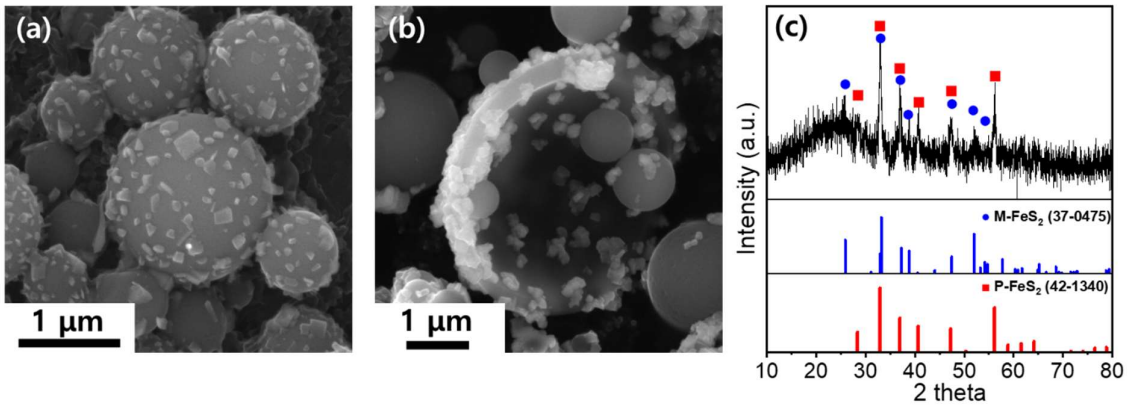


Figure S6. (a,b) SEM images and (c) XRD pattern of Hollow FeS microspheres.

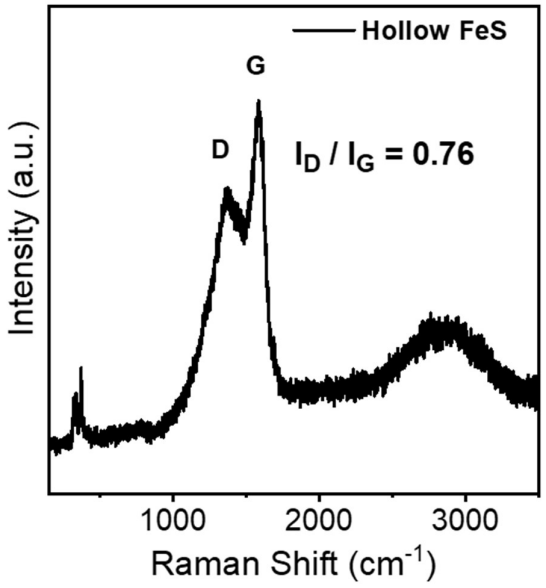


Figure S7. Raman spectra of Hollow FeS microspheres.

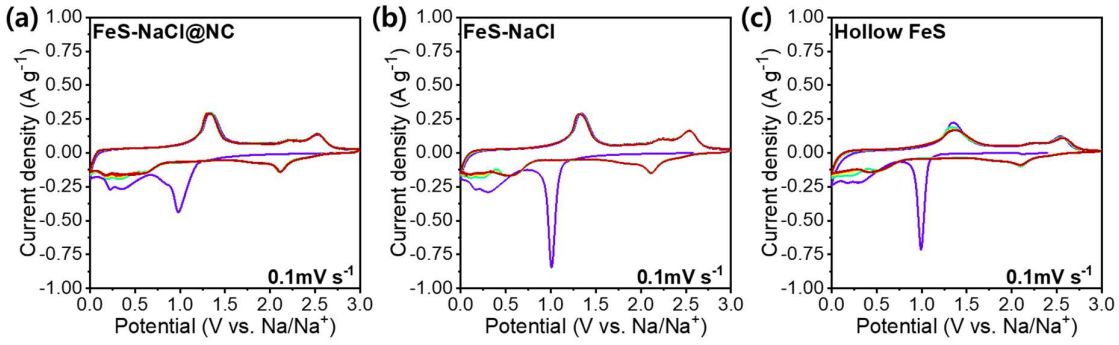


Figure S8. CV curves of (a) FeS-NaCl@NC, (b) FeS-NaCl, and (c) Hollow FeS microspheres.

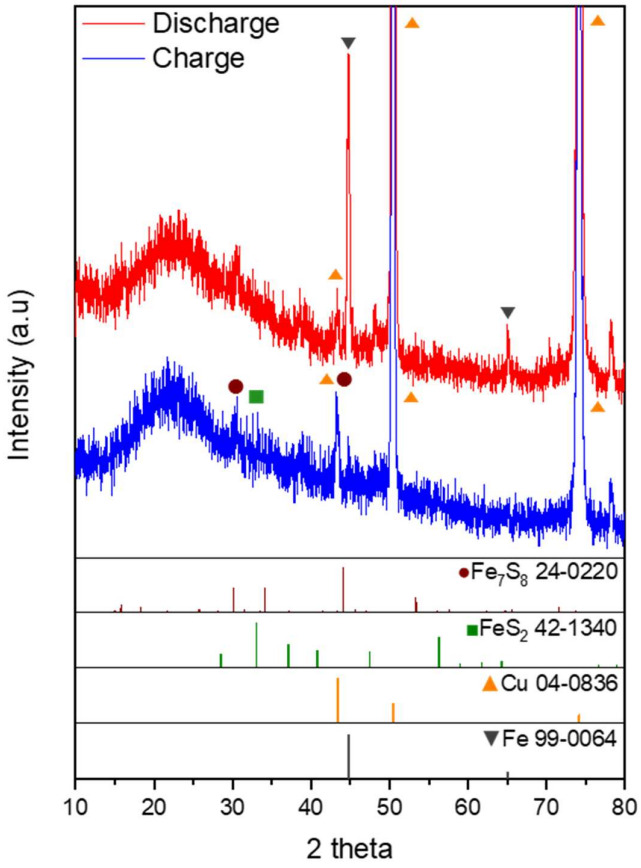


Figure S9. Ex-situ XRD patterns of FeS-NaCl@NC microspheres after the initial discharge and charge processes.

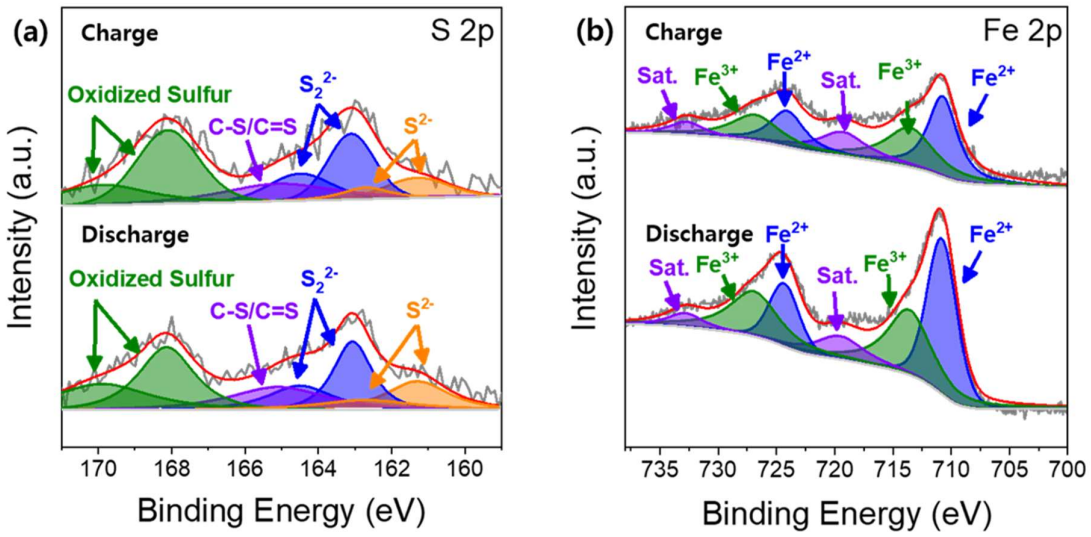


Figure S10. Ex situ XPS spectra of FeS-NaCl@NC microspheres after the initial discharge and charge processes: (a) S 2p spectra and (b) Fe 2p spectra.

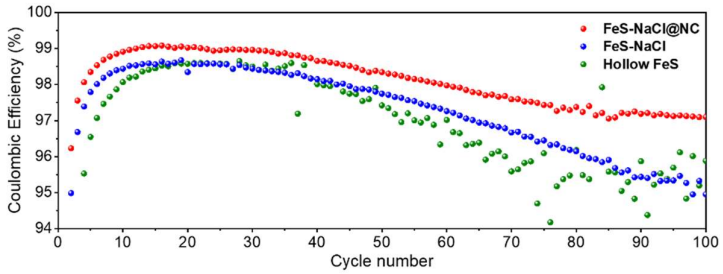


Figure S11. Coulombic efficiency vs cycle number for FeS-NaCl@NC, FeS-NaCl, and Hollow FeS microspheres.

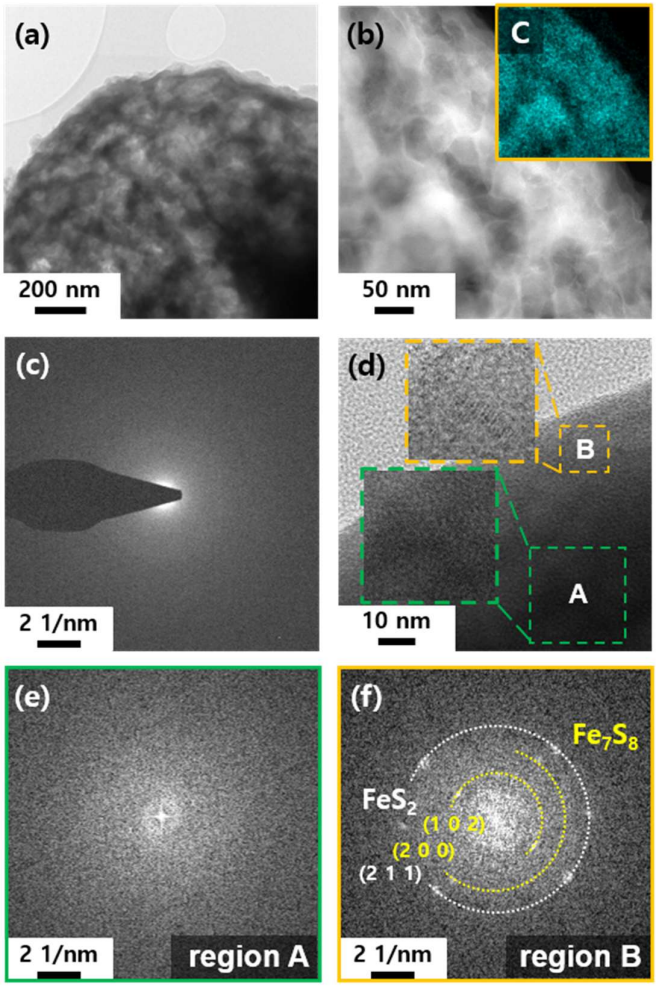


Figure S12. (a,b) TEM images and (c) SAED pattern of the overall FeS-NaCl@NC microsphere after 100 cycles, and (d) HR-TEM image with selected regions A and B, and (e,f) corresponding FFT patterns obtained from regions A and B, respectively.

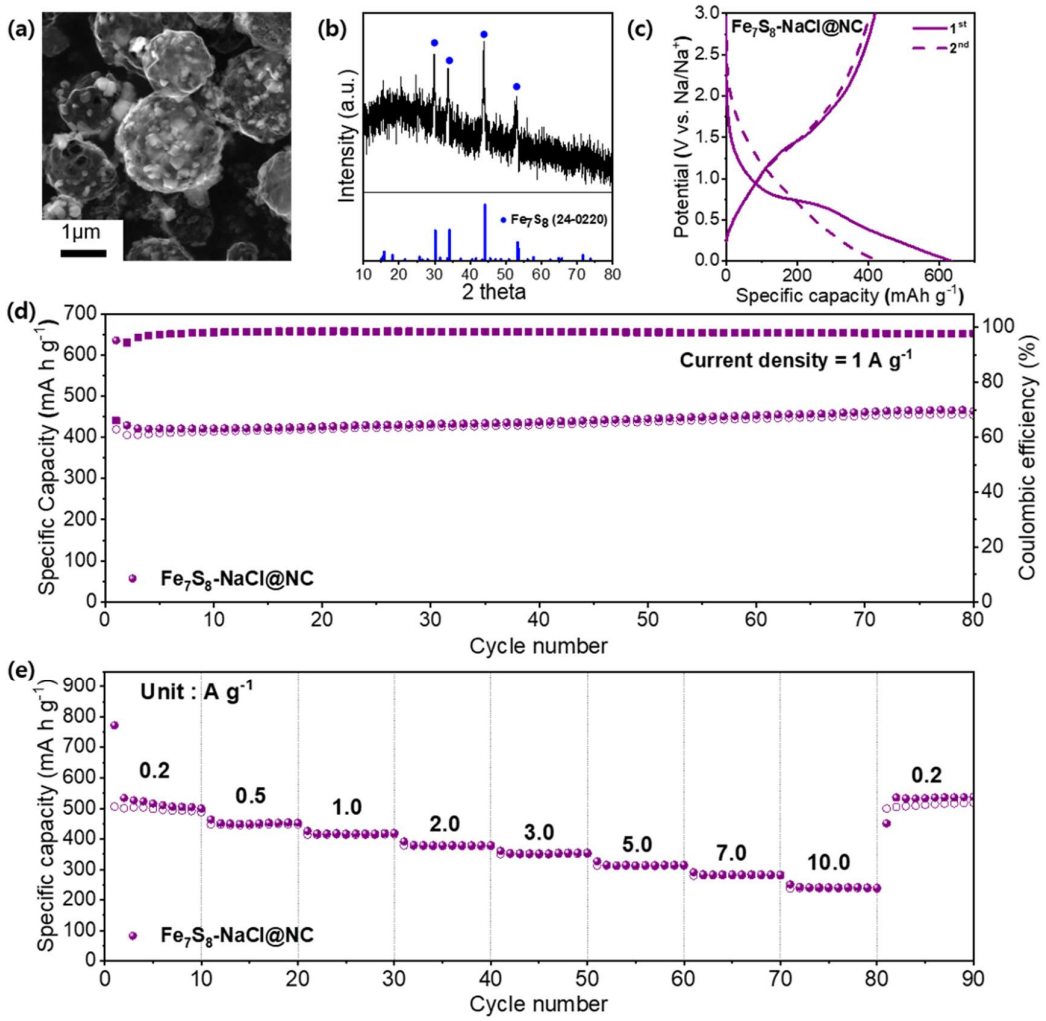


Figure S13. (a) SEM image, (b) XRD pattern, (c) charge-discharge profile, (d) cycle and (e) rate performances of phase-controlled Fe_7S_8-NaCl@NC microspheres.

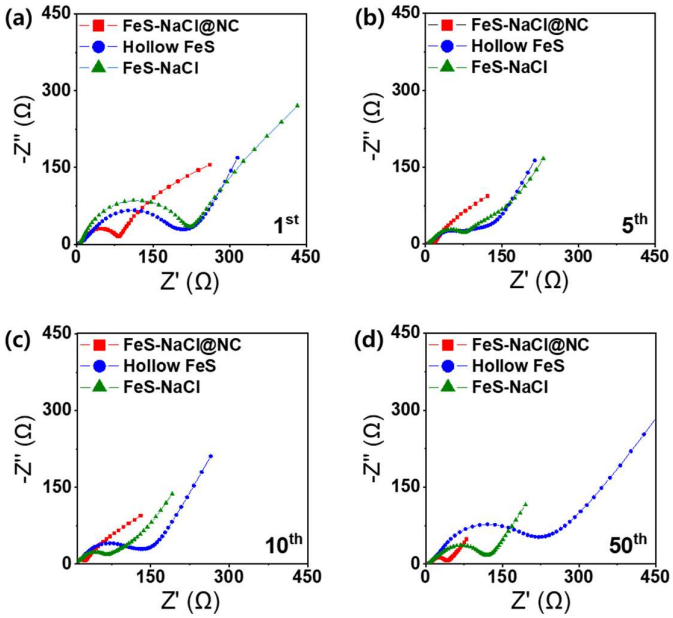
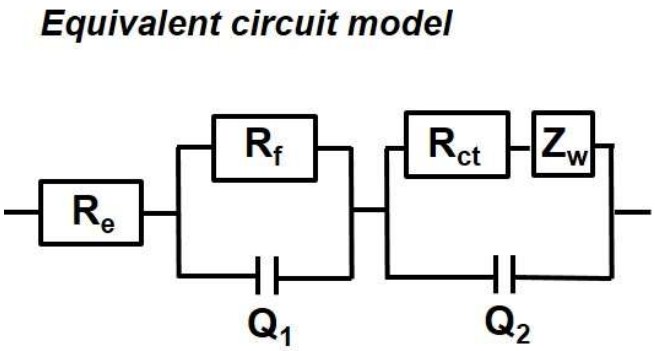


Figure S14. EIS Nyquist plots of FeS-NaCl@NC, FeS-NaCl, and Hollow FeS microspheres for the (a) 1st, (b) 5th, (c) 10th, and (d) 50th cycles.



R_e: the electrolyte resistance, corresponding to the intercept of high frequency semicircle at Z_{re} axis

R_f: the SEI layer resistance corresponding to the high-frequency semicircle

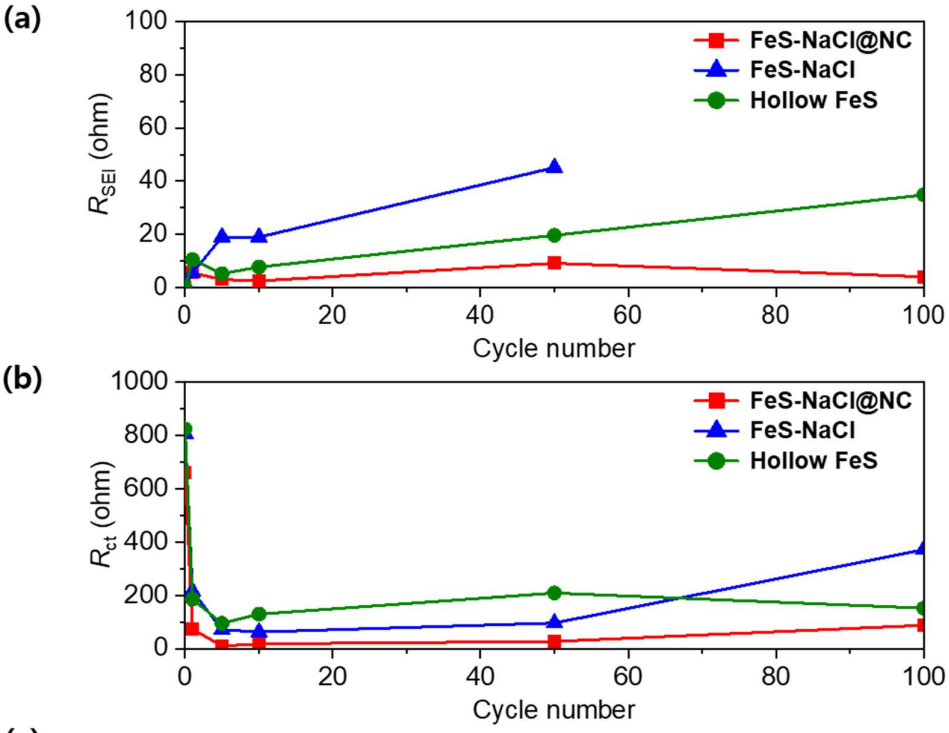
Q_1: the dielectric relaxation capacitance corresponding to the high-frequency semicircle

R_{ct}: the charge transfer resistance related to the middle-frequency semicircle

Q_2: the associated double-layer capacitance related to the middle-frequency semicircle

Z_w: the Na-ion diffusion resistance

Figure S15. Randles type equivalent circuit.



(c)

	R_{SEI} (ohm)		
	FeS-NaCl@NC	FeS-NaCl	Hollow FeS
Fresh	-	-	-
1st	5.5	5.5	10.5
5th	3.0	19.0	5.2
10th	2.5	19.0	7.7
50th	9.1	45.1	19.6
100th	4.0	Not reliably fitted	34.9

	R_{ct} (ohm)		
	FeS-NaCl@NC	FeS-NaCl	Hollow FeS
Fresh	662.4	806.5	824.7
1st	73.4	216.2	186.2
5th	10.0	71.1	94.7
10th	18.1	62.8	129.7
50th	27.1	96.5	208.9
100th	87.7	372.1	152.3

Figure S16. Evolution of (a) R_{SEI} and (b) R_{ct} as functions of cycle number for the FeS-NaCl@NC, FeS-NaCl, and Hollow FeS microspheres, and (c) corresponding resistance values at different cycling stages.

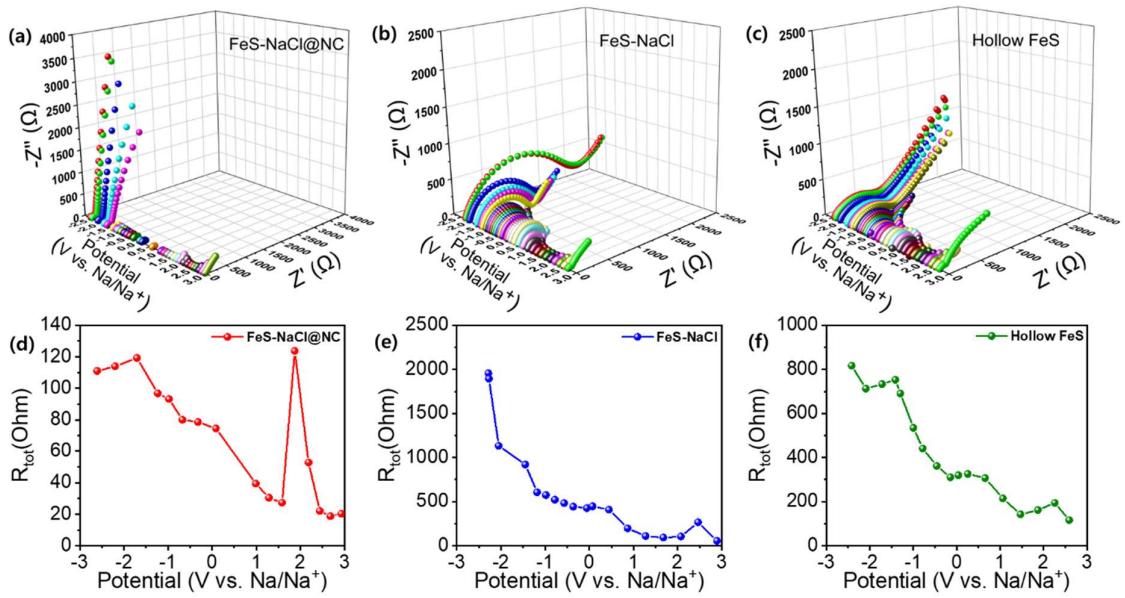


Figure S17. *In situ* EIS characterization of the microspheres: (a-c) Nyquist plots obtained at selected potential during the first cycle, (d-f) R_{tot} vs. potential graph.

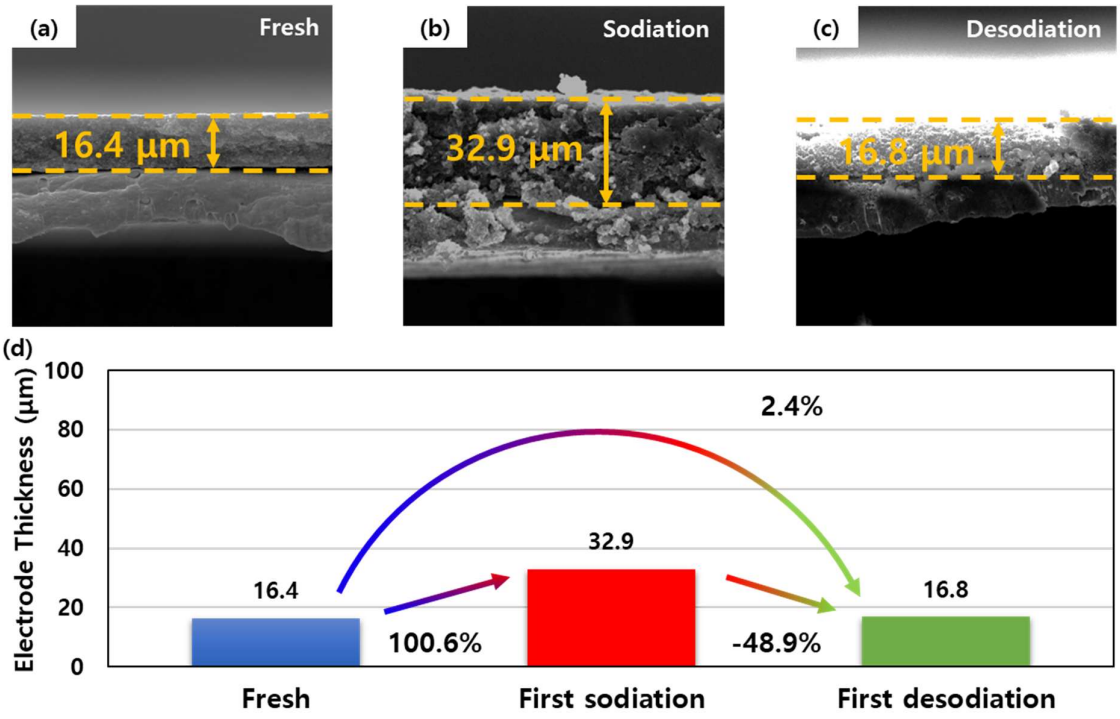


Figure S18. Cross-sectional FE-SEM images of FeS-NaCl microspheres: (a) Prior to cycling, (b) after initial sodiation, (c) after de-sodiation process and (d) electrode swelling rate observed during the initial sodiation/de-sodiation step.

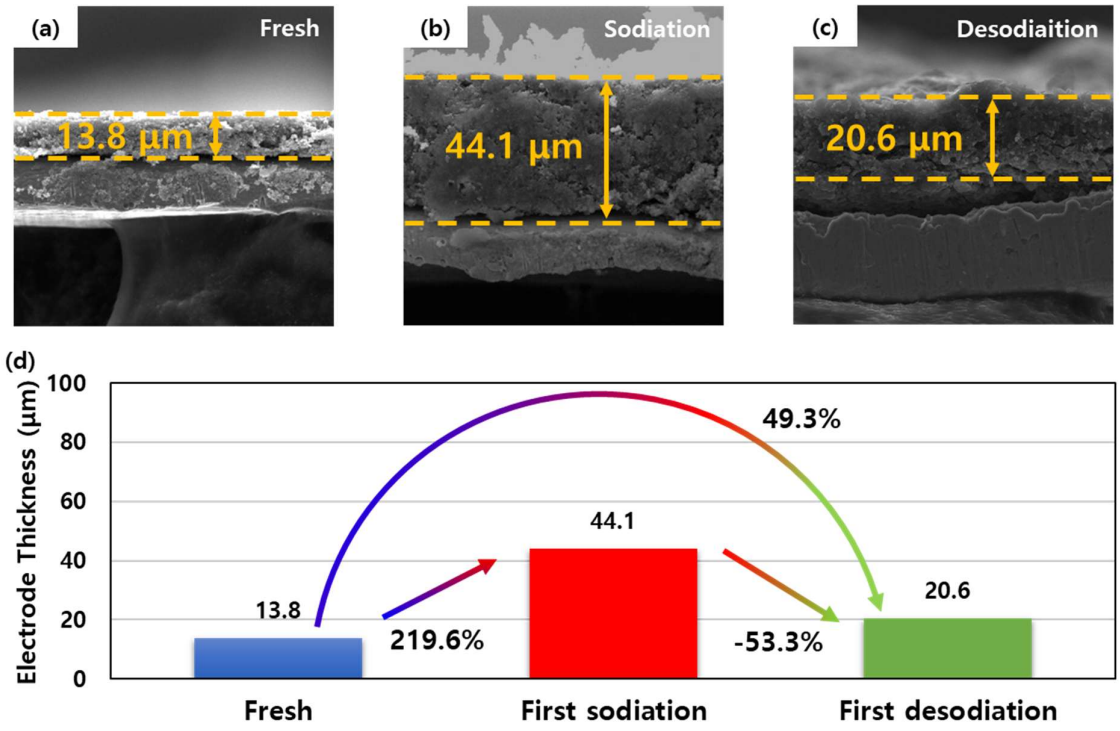


Figure S19. Cross-sectional FE-SEM images of Hollow FeS microspheres: (a) Prior to cycling, (b) after initial sodiation, (c) after de-sodiation process and (d) electrode swelling rate observed during the initial sodiation/de-sodiation step.

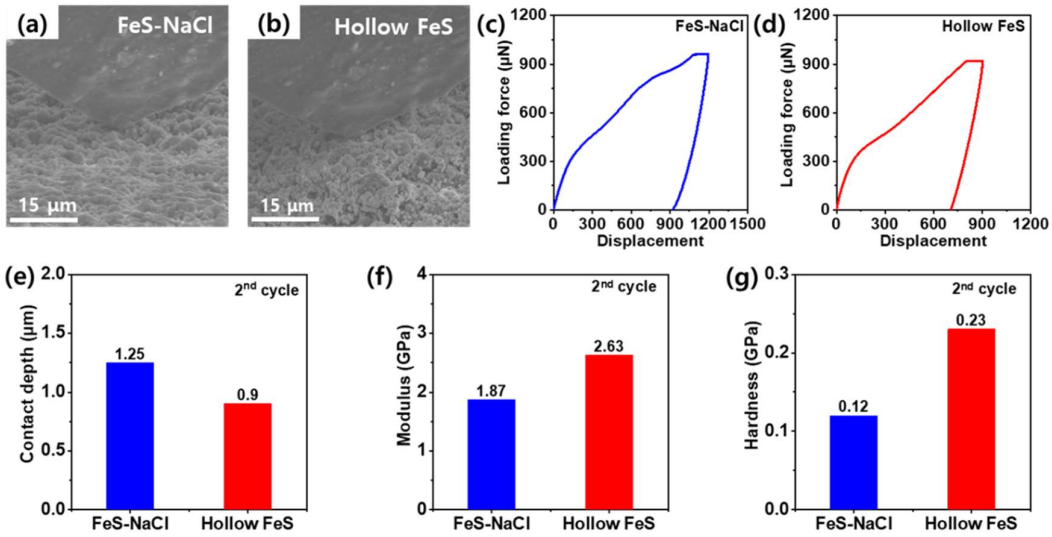


Figure S20. (a,b) SEM images from the nanoindentation analysis of FeS-NaCl and Hollow FeS microspheres. (c,d) Loading force–displacement curves, (e) contact depth, (f) modulus (g) hardness of FeS-NaCl and Hollow FeS microspheres after the 2nd cycle.

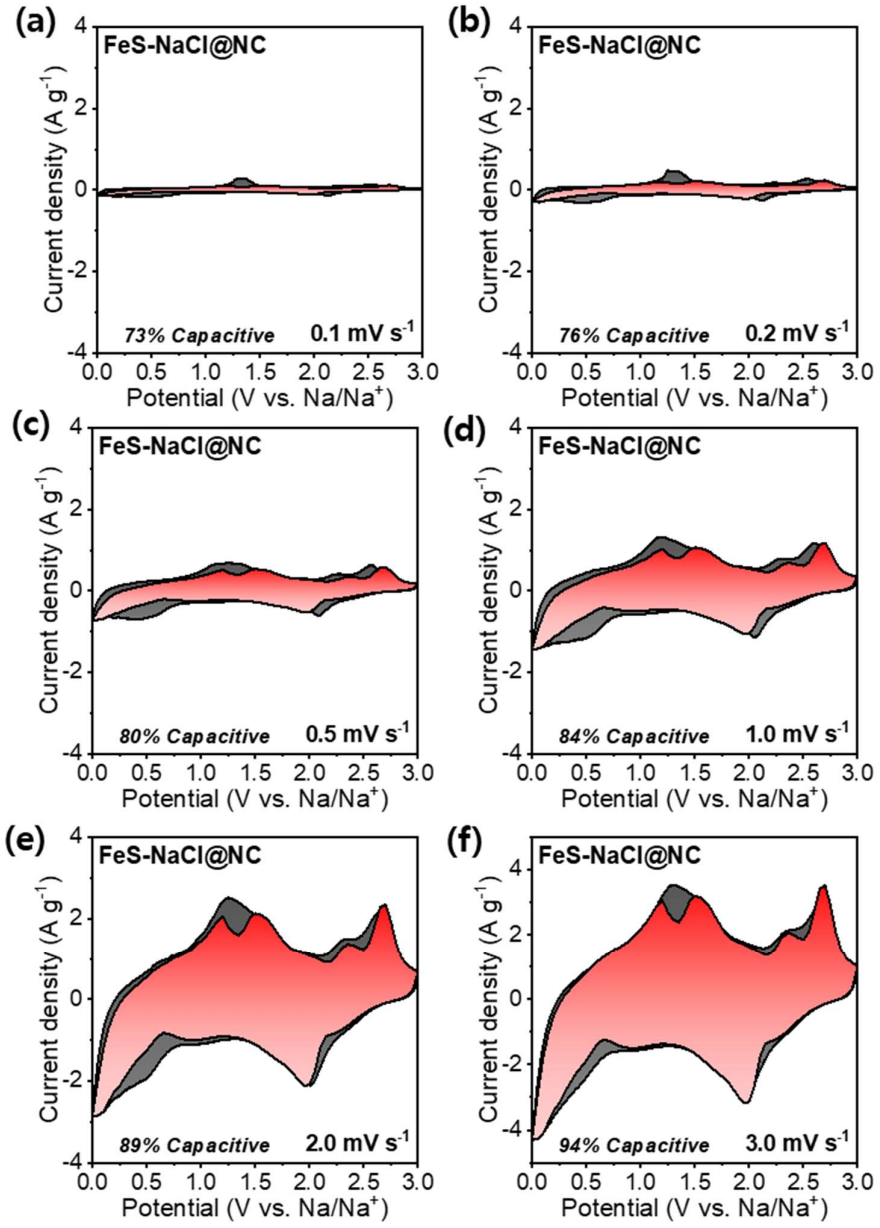


Figure S21. Deconvolution of capacitive and diffusion-controlled current contributions for FeS-NaCl@NC microspheres at various scan rates of (a) 0.1, (b) 0.2, (c) 0.5, (d) 1.0, (e) 2.0, and (f) 3 mV s^{-1}.

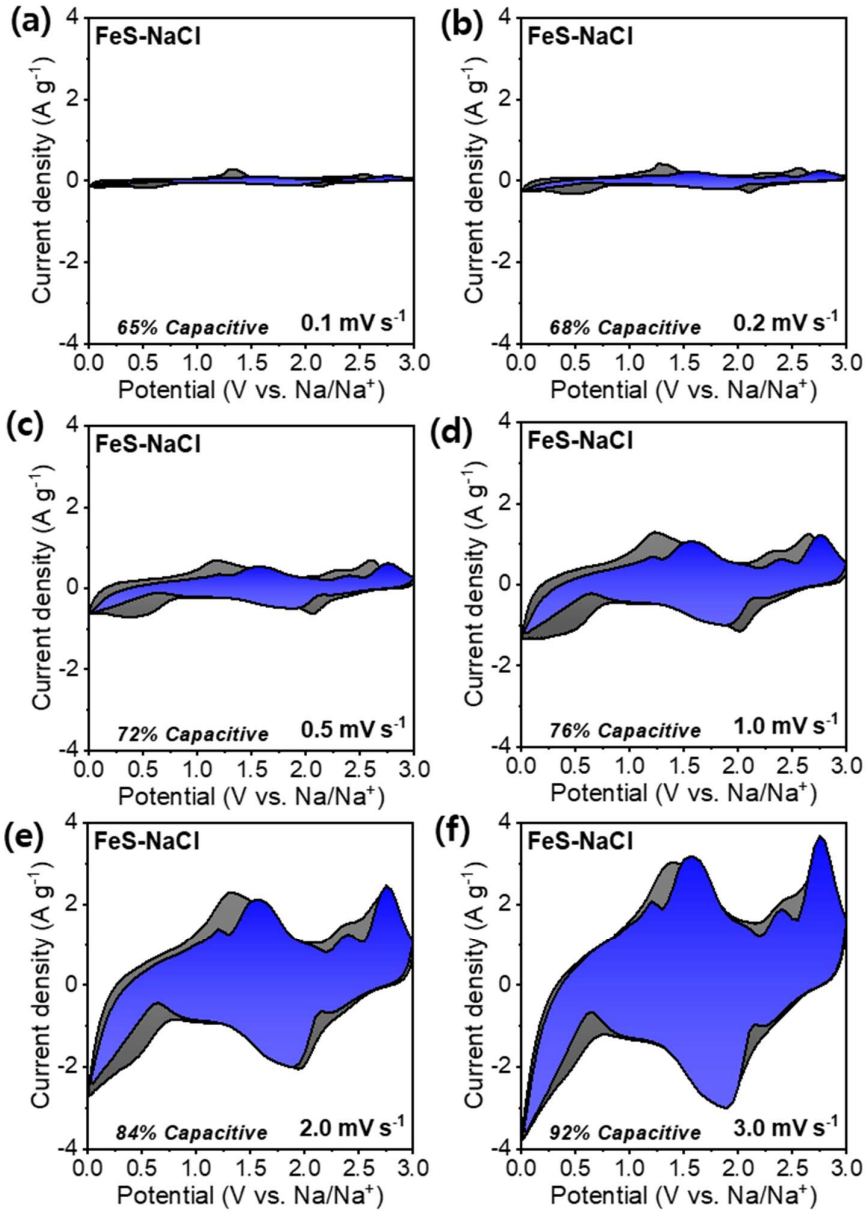


Figure S22. Deconvolution of capacitive and diffusion-controlled current contributions for FeS-NaCl microspheres at various scan rates of (a) 0.1, (b) 0.2, (c) 0.5, (d) 1.0, (e) 2.0, and (f) 3 mV s^{-1}.

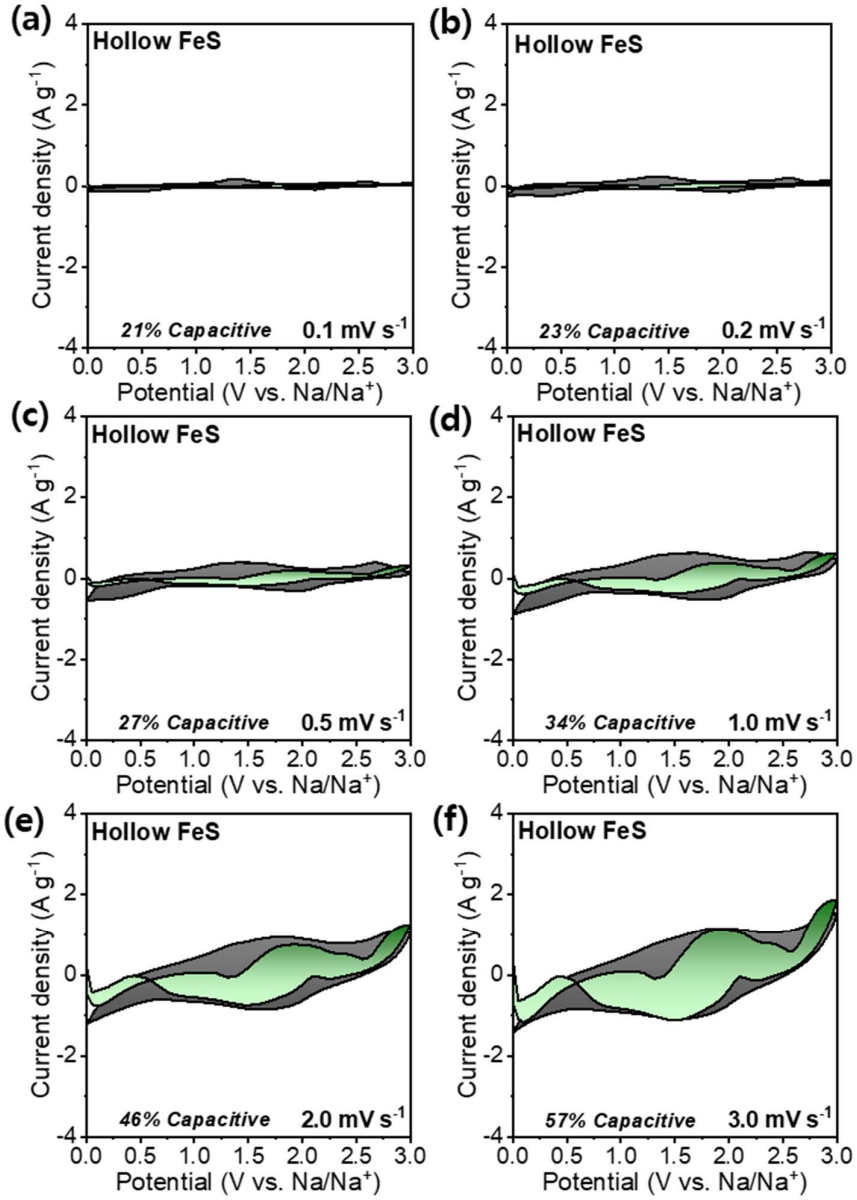


Figure S23. Deconvolution of capacitive and diffusion-controlled current contributions for Hollow FeS microspheres at various scan rates of (a) 0.1, (b) 0.2, (c) 0.5, (d) 1.0, (e) 2.0, and (f) 3 mV s^{-1}.

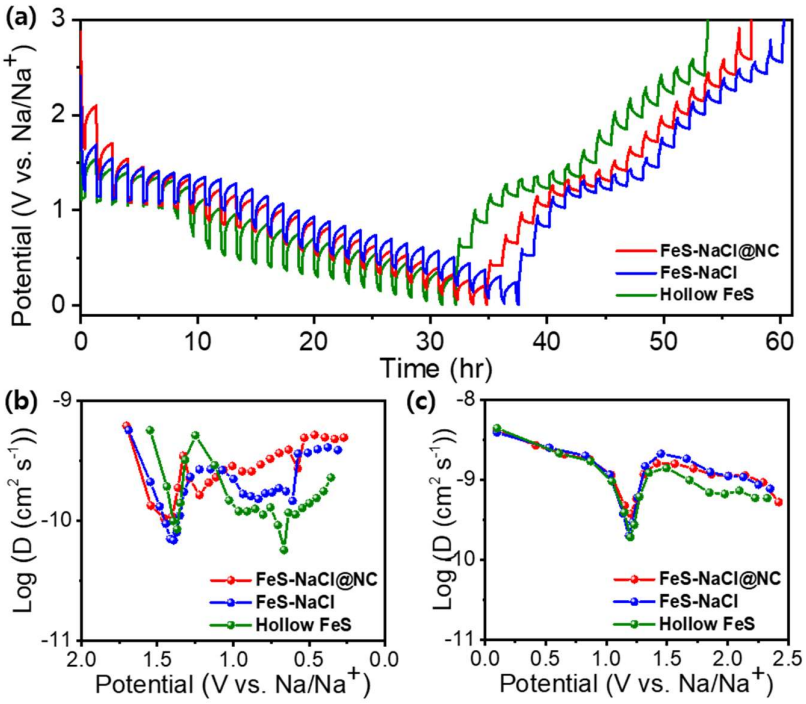


Figure S24. GITT analysis of FeS microspheres: (a) Voltage profiles of FeS-NaCl@NC, FeS-NaCl, and Hollow FeS microspheres during sodiation/desodiation processes. (b,c) Corresponding Na^+ diffusion coefficients as a function of potential during (b) sodiation and (c) desodiation, calculated from the GITT responses.

	FeS-NaCl@NC	FeS-NaCl	Hollow FeS
Current density	0.1 A g^{-1}		
Pulse duration	20 min		
Relaxation time	60 min		
Active material mass	0.00208 g	0.00251 g	0.00155 g
Electrode radius (r)	0.7 cm		
Electrode thickness (t)	0.002 cm		
Electrode/electrolyte contact area	1.54 cm^2		

Table S3. Experimental and calculation parameters used for GITT analysis and determination of the Na^+ diffusion coefficient.

For the calculation, the effective molar volume V_M was estimated from the geometric electrode volume and active-material loading according to

$$V_M = \frac{M_B \pi r^2 t}{m_B}.$$

Accordingly, when the calculated V_M is substituted into the GITT equation, the M_B and m_B terms are canceled.